UPPSALA
UNIVERSITET

*Digital Comprehensive Summaries of Uppsala Dissertations from the Faculty of Science and Technology* 1740

# An X-ray Spectroscopic Study of Perovskites Oxides and Halides for Emerging Devices

DIBYA PHUYAL

ACTA
UNIVERSITATIS
UPSALIENSIS
UPPSALA
2018

ISSN 1651-6214
ISBN 978-91-513-0493-9
urn:nbn:se:uu:diva-364407

Dissertation presented at Uppsala University to be publicly examined in Häggsalen, Ångströmlaboratoriet, Lägerhyddsvägen 1, Uppsala, Friday, 14 December 2018 at 13:15 for the degree of Doctor of Philosophy. The examination will be conducted in English. Faculty examiner: Research Director Manuel Bibes.

**Abstract**

Phuyal, D. 2018. An X-ray Spectroscopic Study of Perovskites Oxides and Halides for Emerging Devices. *Digital Comprehensive Summaries of Uppsala Dissertations from the Faculty of Science and Technology* 1740. 84 pp. Uppsala: Acta Universitatis Upsaliensis. ISBN 978-91-513-0493-9.

This thesis investigates the electronic structures on several perovskite oxide and halide materials with a focus on light harvesting applications. The systematic study of the electronic properties of the transition metal oxides and post-transition metal halides is a key point if one is to understand their properties. The element and site selective nature of several x-ray based spectroscopic techniques are given special emphasis in order to obtain a complete picture of the electronic properties of the compounds in question. Much of the experimental studies are accompanied by *ab initio* calculations that corroborate with our experimental results.

In the oxide portion of this work, a new class of metallic oxides based on doping of an antiferromagnetic $LaFeO_3$ was synthesized and systematically studied with x-ray absorption, x-ray emission, and photoemission spectroscopies. The compound's electronic structure is complex, having itinerant as well as localized components that give rise to a unique physical state where antiferromagnetism, metallicity and charge-disproportionation coexist. Our resonant photoemission results establish that the Fe states in both magnetically ordered oxides show insulting properties, while the Mo states provide an itinerant band crossing the Fermi level. An excitation energy-dependent RIXS investigation on $LaFe_{1-x}Mo_xO_3$ and the double perovskite $Sr_2FeMoO_6$ revealed a double peak structure located in proximity to the elastic peak that is identified to purely *d-d* excitations, attributed to the strongly correlated nature of these transition metal compounds.

The growth of high-quality thin film ferroelectric based on $BaTiO_3$ grown epitaxially by means of pulsed laser deposition were investigated. We systematically reduce the band gap of the ferroelectric thin film while retaining its polarization at ambient conditions in spite of the aliovalent doping. The electronic structure is studied by several x-ray techniques that show how the ferroelectricity persists as well as the effective reduction of the band gap through hybridized states.

In the post-transition metal halides, the valence and conduction bands were mapped using x-ray absorption, emission, and photoemission spectroscopies. The spectroscopic results identify the constituent states that form the valence band as well as the band energy positions, which is an imperative parameter in optoelectronic devices. In addition, x-ray based spectroscopy was used to demonstrate the stereochemical activity of lone-pair states ($5s^2$ and $6s^2$) for several different halide compounds and their influence on the chemical, structural, and electronic properties of the material. Nanostructured halide perovskites are also explored. The position of iodine *p* states and valence band states in reduced dimensional lead-based compounds were examined, as their states are found to be confined in one crystallographic direction in contrast to their three-dimensional counterpart. This information highlights the interesting material properties and their use in current third generation solar cell research.

*Keywords:* perovskite oxides, halide perovskites, x-ray spectroscopy, electronic structure

*Dibya Phuyal, Department of Physics and Astronomy, Molecular and Condensed Matter Physics, Box 516, Uppsala University, SE-751 20 Uppsala, Sweden.*

ISSN 1651-6214
ISBN 978-91-513-0493-9
urn:nbn:se:uu:diva-364407 (http://urn.kb.se/resolve?urn=urn:nbn:se:uu:diva-364407)

*To my family*

# List of Papers

This thesis is based on the following papers, which are referred to in the text by their Roman numerals.

I. Doping induced site-selective Mott insulating phase in $LaFeO_3$
Somnath Jana, Swarup K. Panda, Dibya Phuyal, Banabir Pal, Soham Mukherjee, Anirban Dutta, Puri A. Kumar, Daniel Hedlund, Joahn Schött, Patrik Thunström, Yaroslav Kvashnina, Håkan Rensmo, M. Venkata Kamalakar, Carlo U. Serge, Peter Svendlindh, Klas Gunnarsson, Silke Biermann, Olle Eriksson, Olof Karis, and D.D. Sarma
*Submitted, Nature Communications, 2018.*

II. Electronic structure of the charge disproportionate and metallicity in $LaFe_{1-x}Mo_xO_3$ studied by resonant x-ray spectroscopies
Dibya Phuyal, Somnath Jana, Soham Mukherjee, Håkan Rensmo, Sergei Butorn, and Olof Karis.
*In Manuscript*

III. Valence Electronic Structure of the double perovskite $Sr_2FeMoO_6$ through resonant x-ray spectroscopies
Dibya Phuyal, Somnath Jana, Håkan Rensmo, Sergei M. Butorin, and Olof Karis
*In Manuscript*

IV. The origin of low bandgap and ferroelectricity of a co-doped $BaTiO_3$
Dibya Phuyal, Soham Mukherjee, Shyamashis Das, Somnath Jana, Kristina O. Kvashnina, D.D. Sarma, Håkan Rensmo, Sergei M. Butorin, and Olof Karis.
*Accepted, Europhysics Letters*, G40482/B19376, 2018.

V. Ferroelectric properties of doped $BaTiO_3$ thin film by pulsed laser deposition
Dibya Phuyal, Soham Mukherjee, Somnath Jana, Shyamashis Das, D.D. Sarma, Håkan Rensmo, Sergei M. Butorin, and Olof Karis.
*In Manuscript*

VI. Impact of synthetic routes on the structural and physical properties of butyl-1,4-diammonium lead iodide semiconductors

Majid Safdari , Dibya Phuyal , Bertrand Philippe, Per H. Svensson, Sergei M. Butorin, Kristina O. Kvashnina, Håkan Rensmo, Lars Kloor, and James M. Gardner
*Journal of Materials Chemistry* A, **5**, 11730, 2017.

VII. Electronic Structure of Two-Dimensional Lead(II) Iodide Perovskite: An Experimental and theoretical Study
Dibya Phuyal, Majid Safdari, Meysam Pazoki, Peng Liu, Bertrand Philippe, Kristina O. Kvashnina, Olof Karis, Sergei M. Butorin, Håkan Rensmo, Tomas Edvinsson, Lars Kloo, and James Gardner
*Chemistry of Materials*, **30**, 4959-4967, 2018.

VIII. The electronic structure and band interface of cesium bismuth iodide on a titania heterostructure using hard X-ray spectroscopy
Dibya Phuyal, Sagar M. Jain, Bertrand Philippe, Malin B. Johansson, Meysam Pazoki, Jolla Kullgren, Kristina O. Kvashnina, Matthias Klintenberg, Erik M. J. Johansson, Sergei M. Butorin, Olof Karis, and Håkan Rensmo.
*Journal of Materials Chemistry A*, **6**, 9498, 2018.

IX. An effective approach of vapour assisted morphological tailoring for reducing metal defect sites in lead-free, $(CH_3NH_3)_3Bi_2I_9$ bismuth-based perovskite solar cells for improved performance and long-term stability
Sagar M. Jain, Dibyua Phuyal, Matthew L. Davies, Meng Li, Bertrand Philippe, Catherine De Castro, Zhen Qiu, Jinhyun Kim, Trystan Watson, Wing Chung Tsoi, Olof Karis, Håkan Rensmo, Gerrit Boschloo, Tomas Edvinsson, and James R. Durant.
*Nano Energy,* **49**, 614-624, 2018.

X. Inorganic $CsPbI_3$ Perovskite Coating on PbS Quantum Dot for Highly Efficient and Stable Infrared Light Converting Solar Cells
Xiaoliang Zhang, Jindan Zhang, Dibya Phuyal, Juan Du, Lei Tian, Viktor A. Öberg, Malin B. Johansson, Ute B. Cappel, Olof Karis, Jianhua Liu, Håkan Rensmo, Gerrit Boschloo, and Erik M.J. Johansson.
*Advanced Energy Materials*, **8**, 1702049, 2018.

# Extended Bibliography

The following is a list of publications to which I have contributed, but not included in this thesis.

1. Two-Dimensional flexible high diffusive spin circuits
   Ismael Serrano, Jaganandha Panda, Fernand Denoel, Orjan Vallin, Dibya Phuyal, Olof Karis, Venkata M. Kamalakar.
   *Submitted, Nano Letters, Aug 2018*

2. Investigation of the spectral properties and magnetism of $BiFeO_3$ by dynamical mean-field theory
   Souvik Paul, Diana Iusan, Patrik Thunström, Yaroslav O. Kvashnin, Johan Hellsvik, Manuel Pereiro, Anna Delin, Ronny Knut, Dibya Phuyal, Andreas Lindblad, Olof Karis, Biplap Sanyal, Olle Eriksson
   *Physical Review B* **97**, 125120 2018.

3. Cesium bismuth iodine, $Cs_xBi_yI_z$, solar cell compounds from systematic molar ratio variation
   Malin B. Johansson, Bertrand Philippe, Amitava Banerjee, Dibya Phuyal, Sudip Chakraborty, Mathis Cameau, Huimin Zhu, Rajeev Ahuja, Gerrit Boschloo, Håkan Rensmo, and Erik M.J. Johansson
   *Submitted, ACS Material and Interfaces, 2018*

4. Exchange dependent ultrafast magnetization dynamics in $Fe_{1-x}Ni_x$ alloys
   Somnath Jana, Ronny Knut, Erna K. Delczeg-Czirjak, Rameez S. Malik, Robert Stefanuik, Raghuveer Chimata, Dibya Phual, Venkata Mutta, Serkan Akansel, Daniel Primetzhofer, Martina Ahlberg, Johan Söderstrom, Joahn Åkerman, Peter Svedlindh, Olle Eriksson, and Olof Karis
   *In Manuscript*

Comments on my own participation:

The studies presented in this thesis are the result of collaborations between experimentalists and theoreticians. I have been the responsible person for preparing and preforming x-ray photoemission as well x-ray absorption and emission spectroscopy measurements, treating the experimental data, and writing these relevant sections for all manuscripts. I have been the primary responsible person in fabricating and characterization of thin films as well as spectroscopic results for papers IV and V.

Reprints were made with permission from respective publishers.

# Contents

1 Introduction ........ 11
  1.1 General Overview: Emerging Materials ........ 11
  1.2 Properties of Perovskite Oxides ........ 13
    1.2.1 $ABO_3$ Perovskite Properties and Electronic Structure ........ 13
    1.2.2 Ferroelectric Oxides ........ 16
  1.3 Inorganic-Organic Halide Perovskites ........ 18
    1.3.1 $ABX_3$ Crystal and Electronic Structure ........ 19
    1.3.3 Solar Cell Devices and Interfaces ........ 22
  1.4 Aim of Thesis ........ 24

2 X-Ray Spectroscopic Techniques and Instrumentation ........ 25
  2.1 Basics of X-Ray Spectroscopy ........ 25
    2.1.1 Synchrotron Radiation: Tunable Soft & Hard X-rays ........ 27
    2.1.2 Storage Rings and Insertion Devices ........ 27
    2.1.3 Beamlines and Endstation ........ 28
  2.2 Principles of Photoemission Spectroscopy (PES) ........ 29
    2.2.1 General Formalism: The Photoemission Process ........ 29
    2.2.2 Electron Escape Depth and Photoionization ........ 31
    2.2.3 Resonant Photoemission Spectroscopy ........ 31
  2.3 Principles of X-Ray Absorption and Emission Spectroscopy ........ 33
    2.3.1 Introduction to XAS and HERFD-XAS ........ 33
    2.2.2 X-Ray Emission Spectroscopy ........ 35
    2.2.3 Resonant Inelastic X-Ray Scattering ........ 37
  2.4 Thin Film Fabrication of Ferroelectrics ........ 39
    2.4.1 Pulsed Laser Deposition ........ 39
    2.4.2 X-ray Diffraction and Reflectivity ........ 40
    2.4.3 Piezoforce Microscopy ........ 40

3 Bulk Perovskite Oxides ........ 42
  3.1 Insulator-to-Metallic Antiferromagnetic Oxide: $LaFe_{1-x}Mo_xO_3$ ........ 42
  3.2 Valence Electronic Structure of $LaFe_{1-x}Mo_xO_3$ ........ 45
  3.3 The Double Perovskite $Sr_2FeMoO_6$ ........ 49

4 Bulk and Thin Films of a Doped $BaTiO_3$ ........ 53
  4.1 Low Bandgap and Ferroelectricity of co-doped $BaTiO_3$ ........ 53
  4.2 Thin Film Properties of co-doped $BaTiO_3$ ........ 55

5 Halide Perovskites....59
  5.1 Low-Dimensional Halides....59
  5.2 Lead-Alternative Halide Perovskites....63
  5.4 Nanocrystal Halides....68

6 Outlook....70

7 Acknowledgements....71

8 Populärvetenskaplig Sammanfattning....73

9 References....76

# 1 Introduction

## 1.1 General Overview: Emerging Materials

This thesis targets the development and understanding of emerging materials for fundamental meaning and their connection to early-stage technologies. My objective is to develop an understanding of the electronic and/or magnetic behavior of complex oxides and halide perovskites. This understanding is an essential step to develop new functionalities that can benefit electronic and energy related applications.

It is broadly recognized that the era of microelectronic devices faces many hurdles if it is to meet its expectations outlined by 'Moore's Law' stated in the 1970s[1]. The already exceptional performance of modern electronic devices has transformed much of how society uses and interacts with technology. However, the multitude of scaling limitations with CMOS-based technology and prolific use of communication technology infrastructure necessitates a new era for new electronics. It is predicted that the information and communication sectors and memory electronics will consume as much 40% of global electricity supply by 2030[2]. Therefore, the need for alternative technologies must be envisaged to meet this demand[3,4]. Finding new material systems that can be implemented at a scalable cost, meet the material availability, and integrate into existing manufacturing process is the incentive for much of the academic and industrial research into complex metal oxides today.

Complex oxides have been one of the main pillars of solid-state physics over the last century and continue to offer novel physics. Recent work in oxide electronics suggests it may be plausible to implement such systems at the electronic device level, with potential to reshape computational density and energy-efficiency[5]. This wide range of materials is expanding beyond the scope of integrated electronics into applications previously not emphasized such as photovoltaics[6,7], photocatalysis[8], water splitting[9], and even into health related applications[10]. Advances in thin film deposition, fabrication of heterostructures, and characterization has ushered a new era of complex oxides to that can be harnessed for multi-functional devices.

The other material class investigated in this thesis is perovskite halides for energy-related applications. Halide perovskites have emerged as a serious contender in this field[11,12]. Although silicon and thin film technologies costs have significantly reduced in the last two decades, their fabrication process and materials input to manufacture can still benefit from improvement[13]. Finding alternative materials, with improved performance and simplified engineering, has incentivized the search for new materials that can lower the cost even further. This material class, whose nomenclature is partly adopted from the extensively studied perovskite oxide family, shows exceptional material properties and device performance that is also associated with low-cost solution based fabrication process analogous to the successfully commercialized organic light-emitted diode televisions[14]. The rapid advancement of this material is usually linked to optimization on the elemental composition, high crystal quality, and minimizing defects by achieving sharper interfaces at film junction, and device architecture.

However, several issues need to be resolved to validate this material for commercial relevance. For instance, the stability issues related in the prevailing halide perovskites has remained a concern, as well as the environmental and toxicology hazards of lead[15–18]. This has led to innovations in finding more suitable materials through compositional changes without comprising the outstanding properties of lead-based halides. One route has been exploiting the crystal structure to form lower dimensional variants to the halide perovskites, which has surpassed stability performance of the highest efficiency three-dimensional variety[19]. The other route is the replacement of Pb ions with alternative metals that can retain much of the optical and electrical properties of the best-preforming lead-based materials[20–22].

Since it is established that the electronic structure of perovskite halides are directly linked to some key properties[23,24], this thesis investigates the electronic structures of two emerging routes in halide perovskites: reduced-dimensional systems and lead-alternative materials.

Fundamentally, the development of these emerging materials typically starts from the elemental and atomistic description of the constituent material. The atomic-scale engineering of exotic new materials is mostly of fundamental interest, however the information obtained could serve concrete interest for materials development. A systematic study on the electronic structure of materials such as transition metal oxides and perovskite halides is a key point in understanding their macroscopic properties. This thesis focuses on these challenges in materials research by using x-ray spectroscopic methods. The information from x-ray spectroscopic techniques can offer clues into their electronic structure and underlying chemical and physical mechanisms. In this way, the knowledge obtained from x-ray spectroscopy is indispensible in correlating the electronic structure to the macroscopic properties of emerging materials.

In this chapter, a brief state of the art review about the emerging materials in oxide research and inorganic-organic halides are presented.

## 1.2 Properties of Perovskite Oxides

### 1.2.1 $ABO_3$ Perovskite Properties and Electronic Structure

The bulk transition-metal oxide (TMOs) perovskites have displayed a wide range of phenomena that have generated special interest to experimentalist and theorists alike. Although this class of materials are well-studied[25], their intriguing properties such metal-insulator transitions, colossal magnetoresistance, ferroelectricity, and superconductivity continue to surprise the research community[26–29]. These properties emerge from interactions of electrons in a many-particle system that is principally governed by several competing interactions: charge, spin, lattice, and orbital as shown in Fig. 1.1(a). The most significant of these interactions is the correlation of electrons in perovskite solids, where the interplay between electrons originate from hybridization and localized effects often rooted in electron-electron repulsions[27]. This central parameter to perovskite oxides, the interaction of the 3*d* electrons, can induce ground states with unusual macroscopic characteristics.

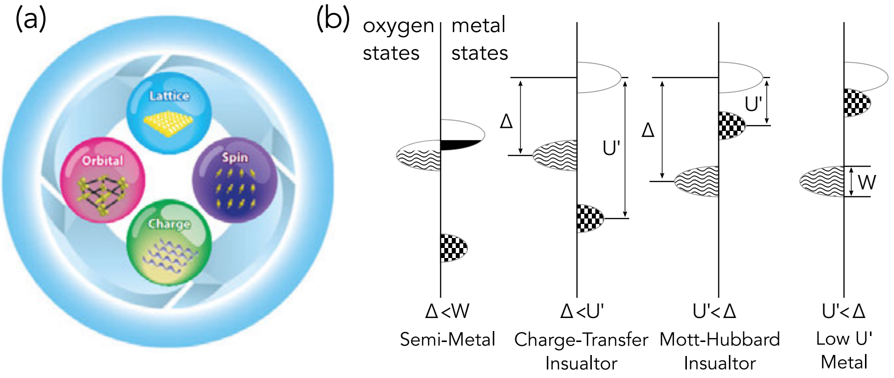

*Figure 1.1* (a) The competing interactions of charge, spin, lattice, and orbital degrees of freedom in transition metal oxides (*Figure adapted from* Ref. [29]) (b) Zaanen-Sawatzky-Allen framework successfully applied to most TMOs based on their *U, W,* and Δ parameters.

The metallic or insulating behavior of oxides has launched systematic studies on the many interactions and correlation in solids. In the standard paradigm of perovskite oxides, the global electronic structure is understood through the competition and/or cooperation by the TM 3*d*-3*d* on-site Coulomb interaction energy known as $U$, the charge-transfer energy from the occupied O 2*p* orbitals to the empty TM 3*d* orbitals denoted by $\Delta$, and the bandwidth $W$. A successful model that identified correlated systems into separate class of materials of many TMOs is the Zaanen-Sawatzky-Allen framework[30], which recognized the critical parameters that predict whether oxides are metallic or insulating[31] as shown on the right panel of Fig 1.1(b). Strong interplay between the bandwidth ($W$), electron-electron repulsion ($U$), and the charge transfer ($\Delta$) between metal and oxygen bands reveal separate classes of materials reflected in these values:

- *Mott-Hubbard Insulators:* The band gap is proportional to $U$ in the case $U \ll \Delta$, where the Coulomb process dominates and reveals an energy gap between inter-site transition metal ion.
- *Charge Transfer Insulator*: This type is among the most common to perovskite oxides, where the band gap is proportional to $\Delta$, in which the lowest excitation is transferring an electron from the O ligand states to the transition metal ion.
- *Intermediate Compounds*: If $\Delta \sim U$, where a competition between both Coulomb and charge transfer excitations exists.
- *Metals:* This class can be divided into two sets: a semi-metal ($\Delta < W$), and the other a soft metal ($U < W$).

Based on this model, it is possible to describe the variation of the band gap of insulators on $U$ and $\Delta$. These properties also are dependent on the composition through doping, as well as long-range changes to the crystal structure through stress, temperature, and external field. This alters the electronic phase diagram and the ground state properties of the comound. A demonstration of this effect is the colossal magnetoresistance observed in $La_{1-x}Sr_xMnO_3$ by doping the antiferromagnetic (AFM) charge-transfer insulator $LaMnO_3$[32]. This electronic reconstruction is associated with a half metallic ferromagnetism that is explained in terms of charge carriers and local spins from Mn 3*d* states[33]. This example is one of many in which a collective phase transition through doping enables oxide materials for interesting fundamentals and for potential use in emerging devices.

As discussed earlier, perovskite oxides have bands that are strongly associated with *d* orbital character. A transition metal (TM) in a crystal structure with octahedral (or several other symmetries) symmetry leads to lifting the degeneracy of *d* orbitals due to the electrostatic interaction with neighboring O 2*p* orbitals. The interaction of a TM ion in a ligand electrostatic field from a quantum mechanical approach is called Crystal Field Theory (CFT). The orbital quantum number for electrons in a $d$ orbital is $L = 2$, thus the degeneracy is $2L+1 = 5$. These orbitals are: $d_{xy}$, $d_{yz}$, $d_{zx}$, $d_{x^2-y^2}$, $d_{3z^2-r^2}$, and are illustrated in Fig. 1.2(a). These orbitals are also distributed preferentially in space and have their distribution maxima in a region in the coordinate axes, depending on the orientation of the lobes. In the octahedral environment, they can be classified in two groups: $d_{xy}$, $d_{yz}$, and $d_{zx}$, which point in between the coordinate axes are known as $t_{2g}$, and $d_{x^2-y^2}$, $d_{3z^2-r^2}$ have a maxima along the coordinate axes, known as $e_g$ orbitals.

When the central TM ion is placed in a non-spherically symmetric electrostatic field, the different $d$ orbitals respond non-equivalently. The energy of the individual $d$ orbital adjusts to this crystal field and shifts according to its orientation in the unit cell. An example of this effect on a TM ion in a octahedron coordination, where the $e_g$ orbitals point toward the oxygen ligands increasing their energy, while the $t_{2g}$ orbitals point in between them, resulting in a lower energy for the latter as shown in Fig. 1.2(b). The residual degeneracy can be lifted even further when considering the coordination (such as tetrahedral, orthorhombic) of the TM ion and the different distortions of the octahedra. The electron filling of these orbitals are complicated further by other interactions such as spin-orbit coupling (LS), Hund's coupling ($J_H$), Jahn-Teller distortions, or other coupled phenomena and beyond the scope of this thesis.

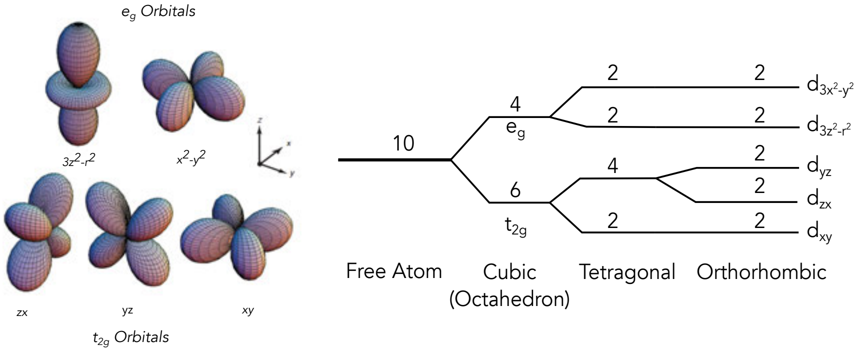

*Figure 1.2* (a) The five-fold degenerate $d$ orbitals in a transition metal ion (*Figure adapted from* Ref. [27]). (b) The crystal field splitting lifts the degeneracy of the $d$ orbitals for different symmetries.

The spectroscopic signatures of electronic phase transitions and the crystal field splitting are explored in this work through several x-ray spectroscopic methods. Photoemission spectroscopy, in particular at the resonant condition, is perfectly suited to qualitatively asses the changes to the electronic ground state of a Mo doped $LaFeO_3$ where we discuss the transition from an insulating to a metallic state as a function of doping. The double perovskite $Sr_2FeMoO_6$, where Fe and Mo occupy alternatively at the B site of the unit cell, is also rationalized through x-ray spectroscopy on its unique coexistence of half-metallic and magnetism. The material properties and the detailed electronic structure results are presented in Chapter 3.

### 1.2.2 Ferroelectric Oxides

Ferroelectric materials possess a spontaneous electrical polarization that can be switched with an external electrical field. This stable ground state is due to a minimized free energy configuration with a double potential well that is the result of a phase transition from an ordinary dielectric to ferroelectric at the Curie temperature ($T_C$) as shown in Fig. 1.3(a). The most distinguishing feature of ferroelectrics is the possibility to switch the spontaneous polarization by an applied field. The spontaneous polarization of ferroelectric materials implies a hysteresis effect, which can be used as a memory function[34], shown in Fig. 1.3(b). It is noteworthy that the FE polarization has a remnant polarization ($P_R$) after the sweeping of electrical voltage, similar to the magnetic analogue in ferromagnetic materials.

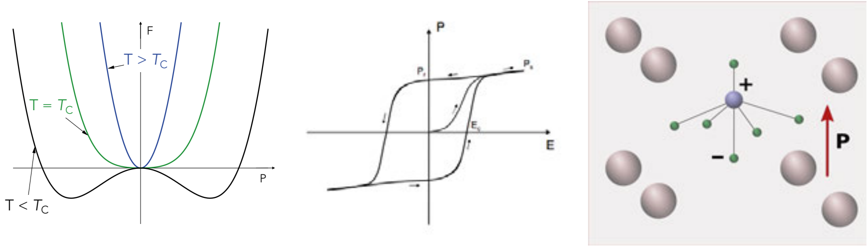

*Figure 1.3* (a) The free energy (F) is plotted as function of polarization for T > $T_c$, T = $T_c$, and T < $T_c$ (b) Schematic of a polarization hysteresis loop for a typical ferroelectric in a coercive field ($E_C$), the spontaneous polarization, $P_S$, and the remnant polarization, $P_R$. (c) The off-centering of the Ti ion in BTO, where the polarization **P** points in the direction of the ion displacement.

$BaTiO_3$ (BTO) is a prototypical ferroelectric oxide and is a special interest for its room temperature polarization and used in many applications such as data storage, photovoltaics, transducers and actuators among others[35]. The phase transition is from a high-temperature cubic dielectric to a tetragonal ferroelectric at T ~ 400 K, and orthorhombic to rhombohedral at 190K. The origin in the phase transition from a cubic structure dielectric to a non-centrosymmetric tetragonal phase at $T_C$ is accompanied by a off-centering of the smaller Ti cation, where the spontaneous polarization derives largely from the electrical dipole moment created by this shift[36]. The resulting polarization is directed along the *c* axis, in the same direction as the Ti ion displacement (see Fig. 1.3(c)). This phase shift is accompanied by changes to the local structure and overall covalency, where the significant hybridization between Ti 3*d* states and O 2*p* states is essential in stabilizing the ferroelectric distortion[36]. The lowest energy transition in the charge transfer-type insulator is from the strongly mixed Ti *d* - O 2*p* states to unoccupied Ti 3*d* bands with a gap ($E_g$) of 3.2 eV. The Ti $d^0$ configuration is reasoned to be a necessary condition for B cation displacement, as other Ba$M$O$_3$ ($M$ = Mn, Fe, Co, etc.) oxides with formally occupied $d^n$ states at the metal site retain their inversion symmetry[37]. The formal valency at the *d* site in is also concomitant with magnetic order, as *d* orbital occupancy is requirement for magnetic moments. However, the $d^0$ and $d^n$ formal valency tend to compete for ferroelectric and ferromagnetic order, with only a few room temperature materials with a coupled ordering[37].

Another extraordinary property of ferroelectric oxides is the ability to generate a bulk photovoltaic effect (BPVE)[38]. Under illumination, they exhibit a photocurrent that is parallel to the polarization direction. Although ferroelectrics usually have a large optical gap, they have recently shown remarkable results that have attracted the attention of the photovoltaic community. Recent experiments showed that a Cr doped BiFeO$_3$ (a room-temperature ferroelectric with weak magnetism) in a planar device architecture under illumination showed an efficiency of 8.1 %[7]. The BPVE in ferroelectrics is also able to generate a photovoltage that is larger than the bandgap[39]. BTO was shown to produce a photovoltage of 8.1 V and efficiency of 4.1%[40]. There is a serious push to improve upon this work with low bandgap ferroelectrics, improved thin film deposition, and domain structure manipulation. This groundbreaking work has pushed the field of photoferroics into new focus and attention of broader research disciplines.

In this work, we investigate the effects of compositional changes to the overall electronic structure on a co-doped BTO discussed in Chapter 4. The intentions are to reduce the overall change transfer gap by mixed valence doping at the B site of BaTiO$_3$ with a $d^0$ and $d^n$ metal cations respectively. The substitution at the B site and its effects on its electronic structure are explored with complementary x-ray techniques to reveal the nature of bandgap tuning and effects on polarization.

## 1.3 Inorganic-Organic Halide Perovskites

Inorganic-organic hybrid perovskites halides (HPs) have emerged as a leading contender in the field of low-cost high efficiency solar cell materials. The key attributes to their emergence in solar cell technology is arguably due to its strong optical absorption, long-range electron-hole diffusion lengths, and reasonable mobility of charge carriers, culminating to a high photovoltaic efficiency - all achieved within the past decade[12,41,42]. The primary compound in this large class of materials is $MAPbI_3$ ($MA = CH_3NH_3$), which has a low bandgap of 1.55 eV and a notable efficiency of 12.1% during its early stages of development in 2012[43]. The efficiencies since then have risen dramatically to above 22% in a chemically-substituted compound[44] that now qualify this material for its place in the market with established technologies like silicon and thin film technologies (like CdTe and CIGS). A diverse range of synthesis methods has been used to fabricate devices, most commonly using low-temperature methods. These materials have also attracted attention for its cluster of fundamental scientific discoveries that are addressed in several reviews[12, 45–47].

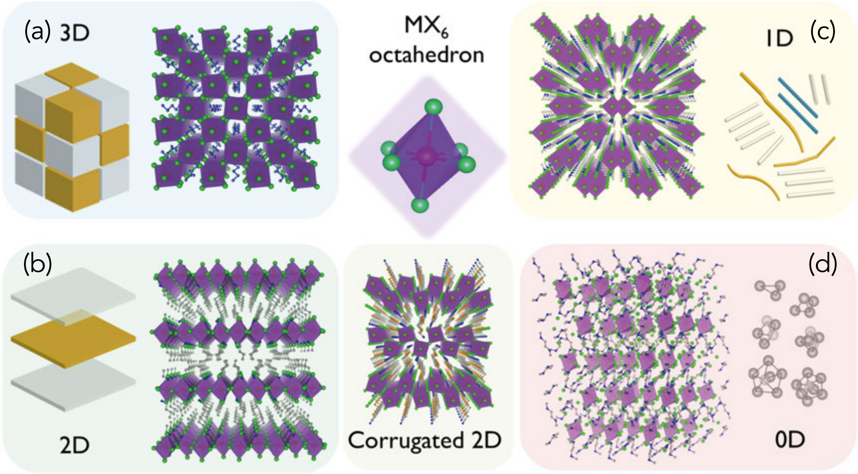

*Figure 1.4* The exceptional structural flexibility of hybrid perovskites enables the formation of various types of structures that strongly depend on both composition and synthesis procedures (a) prototypical 3D $ABX_3$ cubic structure (b) 2D layered structures separate the inorganic $MX_6$ octahedron, (c) 1D nanowires in which metal-halide octahedrons are connected in a chain, and (d) nanocrystals where metal-halide octahedrons are completely isolated (*Figure adapted from* Ref. [47].)

The efficacy of these materials in solar cell devices has given ground to further optimizing this material for commercialization. This has also led to finding alternative variations to inorganic-organic perovskites to achieve comparable materials for high efficiency photovoltaics, such as exploiting the tremendous flexibility to obtain various types of crystal structure as shown in Fig. 1.4. A promising trend is in layered HPs, colloidal nanocrystals, and lead-alternative perovskites – which are all material systems investigated in this thesis. This subset of HPs has unique material characteristics and good device performance of their own, and could individually find their place in future optoelectronic devices.

The subsequent section reviews the chemical and electronic structure of HPs and its different variants. The bulk electronic structure is reviewed and a significant portion of the experimental work in this thesis. The common device architectures in solar cell devices and the role of interfaces are also briefly addressed.

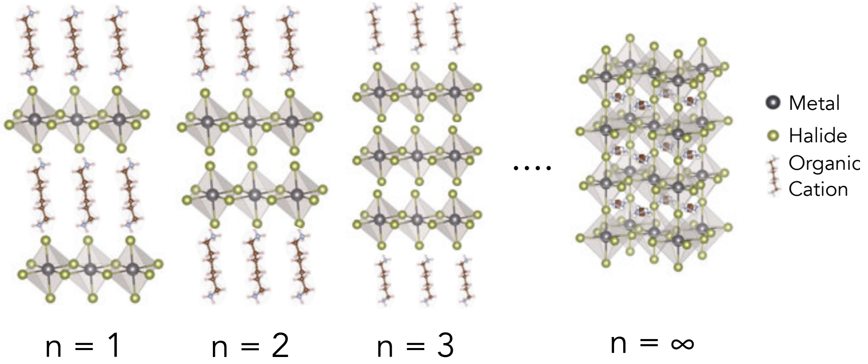

*Figure 1.5* As the tolerance factor deviates from the ideal $t$ = 1, the size restriction on different cations and anions are lifted to form two-dimensional derivatives.

## 1.3.1 ABX$_3$ Crystal and Electronic Structure

Hybrid organic-inorganic perovskites take their nomenclature from its crystal structure that is similar to the CaTiO$_3$ oxide perovskite (ABO$_3$). The most prominent and well studied material in this class is MAPbI$_3$, shown on the far right in Fig. 1.5 A number of exciting physical properties, like colossal magnetoresistance, ferroelectricity and superconductivity, have all been discovered in this prolific family of compounds during the past century[48]. For the ‘hybrid’ perovskites, ones with both inorganic and organic cations, are usually either methylammonium (MA$^+$ = CH$_3$NH$_3$$^+$) or formamidinium (FA$^+$ = CH(NH$_2$)$_2$$^+$), large monovalent cations that fill the octahedral interstitials. The all-inorganic compounds usually contain cesium or recently even rubidium (Rb) at the A site. The B site is usually a post-transition metal (Pb, Bi, Sb, or Sn) and located at the center of the body of an octahedral cluster. The octahedral, $[PbI_6]^{4-}$ unit can form three-dimensional (3-D), two-dimensional (2-D), one-dimensional (1-D) or zero-dimensional (0-D) networks (*see* Fig. 1.4). The anion component is usually a halide element (I, Br, or Cl), making the combinatorial possibilities of this compound numerous. This versatility in this class of hybrid materials allows a vast space to explore new materials with new and useful properties.

The ideal cubic structure for perovskite halides ($AMX_3$) has 6-fold coordination within the octahedron and the A cation in a 12-fold cuboctahedral coordination. The crystallographic stability and probable structure is empirically deduced by considering the well-established Goldschmidt's tolerance factor[49], a ratio of the interatomic distance in an idealized solid-sphere, $t = R_A + R_X/2\sqrt{R_A + R_X}$. The slight differences in the A-X and M-X ionic radii are stringent and a large mismatch can introduce buckling and distortions to the equilibrium structure[50]. This generally produces a lower-symmetry distorted version of the ideal cubic structure, which in turn can manifest a variety of structures with a different set coordination numbers to the A and B cations. Aside from the constraints on the ionic radii, the charge balance and valence assignment can further be extended to attain new polymorphs[50].

Given that there are chemical and physical constraints to achieve a 3D structure, the substitution of various cation and anion sizes allows for remarkable structural tunability. This can result in deviations in the octahedral size and tilt, as well reduced dimensionality mediated by inorganic layers separated by a cation. In two-dimensional perovskites, where size restrictions on the A site cation is relaxed, can result in structures with a different layering of the inorganic layer in between the organic chain. The charges in two-dimensional (2D) materials are restricted in their movement to the two-dimensional plane; however, their confined structure allows one to tune the optical and electronic properties by varying their thickness (*see* Fig. 1.5). This is usually given an index number to the stoichiometry of the material, $R_2(CH_3NH_3)_{n-1}M_nX_{3n+1}$, where R is an organic group, M the divalent transition metal, X is a halide, and n refers to the number of metal halide layers between the long chain organic cation layers. This structure converges to a 3D structure with $n = \infty$, where the ending compound narrows the bandgap and/or increases the mobility of charges within the layers[51]. Although their efficiencies have not matched the 3D equivalents, their improvement is ongoing and efficiencies of 15.3% were reported using $n = 3$ inorganic sheets separated by an organic cation[19]19. The major advantage of 2D HPs over the 3D counterparts is their stability to moisture, which is a serious impediment for successful commercialization of 3D HPs.

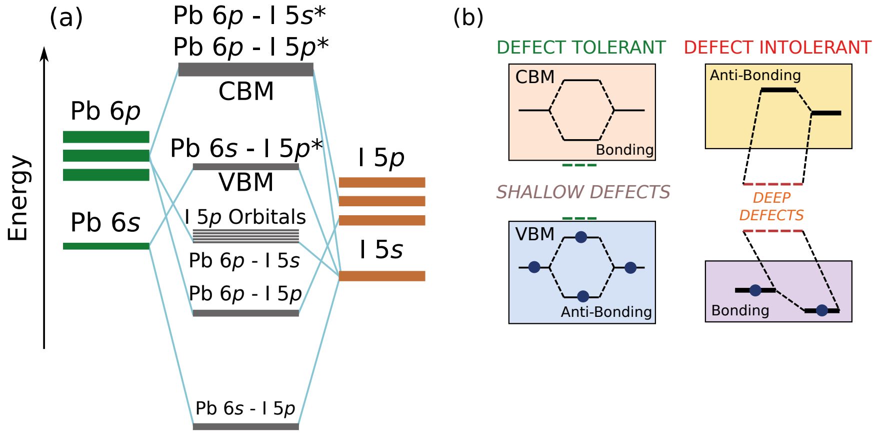

*Figure 1.6* (a) Electronic structure and bonding structure common to most perovskite halide compounds. (b) The antibonding states at the top of the valence band maximum give rise to shallower defects.

The basic electronic structure of the simplest and well-studied perovskite $MAPbI_3$ is partly understood[23,52]. Early studies using density functional theory (DFT) calculations showed the inorganic $PbX_6$ octahedra to have an electronic configuration based on Pb: $5d^{10}6s^{2}6p^{0}$ and I: $5p^{6}$. The Pb $6s/6p$-I $5p$ interactions are responsible for the chemical bonding and form the valence and conduction bands as shown in Fig. 1.6. Arguably the most important property of a light absorbing material is the bandgap ($E_g$), which is directly related to the interaction of frontier electronic states of the constituent compounds. For HPs, the valence band maximum (VBM) is formed of an antibonding (σ*) Pb 6*s* – I 5*p* interactions, while the conduction band minimum is by empty Pb 6*p* and non-bonding Pb 6*p* - I 5*p* interactions, as shown in Fig. 1.6(a). The molecular states stemming from the organic or inorganic A cation lie deeper in the VB and do not hybridize with the inorganic units ($PbI_6$ for example) and lack any significant electronic interaction. Although they do not contribute directly to band edge states, they do influence the crystal structure framework, including the symmetry and bond lengths of the $PbI_6$ octahedra and stability of the HPs thin films.

This configuration of the electronic structure has led HPs to obtain strong optoelectronic properties including characteristic known as defect tolerance[21]. One of the proposed mechanism by which defect tolerance occurs is the presence of antibonding interactions at the VBM, which tends to confine defects to shallow states at the band edges or outside the gap rather than deep in-gap states that act as recombination centers[21], as shown in Fig. 1.6(b). Several authors have argued that the key to properties such as defect-tolerant solar absorbers is due to the bonding structure of the lone pair $ns^2$ hybridization at the B site of HPs crystal structure[53]. In the perovskite structure, a stereochemically active lone pair (or *s*-orbital hybridization) generally gives rise to structural distortions such as bond lengths and bond angles among other properties[54]. Materials currently of interest with this configuration are $Pb^{2+}$, $Sn^{2+}$, $Ge^{2+}$, $Sb^{3+}$, and $Bi^{3+}$, a few of which are discussed in the results section of this thesis.

Although lead-based perovskites have demonstrated the best performance so far, its toxicity and stability present a significant challenge to commercialization. This obstacle has spurred theoretical and experimental research into lead alternatives as a path to overcome the issues pertaining to lead that can deliver comparable material and devices properties that improve upon the toxicity and stability. A few different compositions are explored in their electronic structure in relation to the $MAPbI_3$ analogue, namely with substitutions with the trivalent $Bi^{3+}$ and $Sb^{3+}$ halides that also have a similar lone pair configuration ($ns^2$).

The final class of HPs investigated in thesis takes the form of nanometer-sized nanocrystals (or quantum dots). Recently, they have attracted a diverse set of material science research with promising results in photovoltaic applications, with photovoltaic efficiencies reaching 10.1 %[55]. In general, nanocrystals less than 20 nm are quantum-confined in all three directions, and the improved photophysical properties are accredited to nanoscale effects from quantum confinement[56]. The perovskite quantum dots have garnered attention due to its excellent photophysical properties, bandgap tuning, and high quantum yield of luminescence[57]. Due to the favorable lattice matching between metal halide perovskite and the cubic rock-salt PbS, perovskites have emerged as a preferred material for surface passivation forming a core-shell type structure[58]. $CsPbI_3$ nanocrystals coated directly on PbS quantum dots and its surface electronic structure using photoelectron spectroscopy is presented in Chapter 5.

### 1.3.3 Solar Cell Devices and Interfaces

The most common solar cell architecture for HPs materials are based on the classical dye-sensitized solar cell design with carefully selected layers for efficient charge generation and collection as shown in Fig. 1.7. The principles of operation of this device involve many competing factors and readers are suggested to several reviews for an in-depth analysis[11,59,60]. In brief, the operation involves the (1) the generation of electron-hole pairs (excitons) in the HP absorbing layer, (2) injection and separation of electron-hole pairs into selective n-type electron acceptors and a p-type hole-transport layers (HTM), (3) and subsequent diffuse of carriers through transport layers to electrodes where they simultaneously generate a voltage and current to the external circuit. This simple heterojunction can be adapted to a broad range of materials and fabrication techniques. The promise in this device architecture is the prospect for low manufacturing costs associated with an all-solution based fabrication.

A key function in device operation is the efficient separation and transfer of electron-hole charge carriers at the interfaces in adjacent layers. A crucial requirement is the matching of electronic energy levels between the perovskite absorbing layer and adjacent n-type and p-type layers with minimal energy loss. This should facilitate the efficient and faster charge separation of charges to avoid recombination at the interface, which dramatically hinders the efficiency of the cell. The interface energetics is also crucial to determining the limitation in the open-circuit voltage[60].

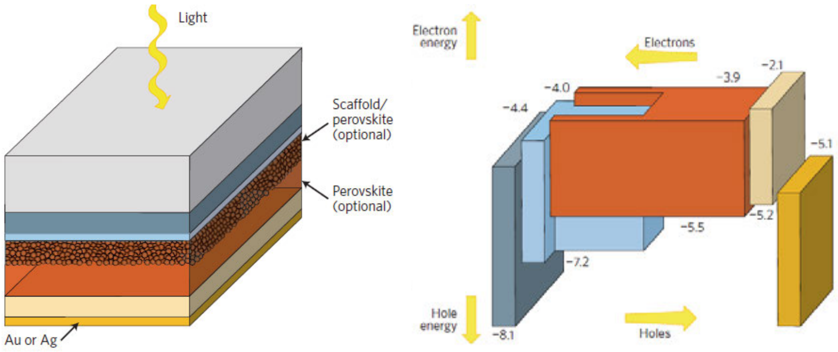

*Figure 1.7* (a) The most commonly used planar heterojunction architecture where the photoactive HP layer is adjacent to selected electron and hole transport layers (light blue and tan respectively). (b) The favorable kinetics necessary to drive efficient electron-hole carriers to reach the electron transport layer and hole transport layer. (*Figure adapted from* Ref. [11]).

The valence and conduction band maximum (VBM and CBM respectively) positions of the absorbing and electron and/or hole conducting layers are shown in Fig. 1.7(b). The *n*-type electron accepting layer CBM has be to higher in energy, i.e. the band offset, to facilitate efficient separation and injection of electrons and lower in energy for holes to the HTL. This energy scheme can be appropriately identified with x-ray photoelectron experiments, and the obtained information can help guide the design of high performance structure. The thesis presents quantitative information on the interfacial energetics for several different perovskite halide systems discussed in the previous section.

## 1.4 Aim of Thesis

The aim of this thesis is to develop an understanding of the electronic structure of these emerging materials through several x-ray spectroscopic techniques. The electronic structures can elucidate much of the observed properties seen in halides and oxide perovskites and guide in materials design. The aim of this chapter has been to introduce the most essential concepts into the materials and the motivation in their research.

Chapter 2 presents the experimental techniques used in this thesis and their abridged formalism. Chapter 3 presents the development of a new material with a rare combination of magnetic order and metallicity, and is demonstrated with extensive electronic structure evidence. Chapter 4 focuses on the development a new low bandgap ferroelectric and how it attains its properties, which is established through various x-ray spectroscopic techniques. The fabrication of thin film and its properties are also presented. Lastly, Chapter 5 discusses the results on halide perovskites supported with theoretical calculations.

# 2 X-Ray Spectroscopic Techniques and Instrumentation

In this chapter, I will present the different experimental methods used to conduct x-ray spectroscopy measurements. The basic formalism of x-ray spectroscopy is briefly reviewed. This section also summarizes the thin film fabrication by pulsed laser deposition and thin film characterization techniques.

## 2.1 Basics of X-Ray Spectroscopy

The aim of x-ray spectroscopy is to obtain information about the electronic structure of a system. The complexity of x-ray interaction with matter offers many spectroscopic routes to bear information to the materials electronic structure, crystal structure and spatial ordering, magnetic ordering, and much more. Since it is possible to obtain chemical and physical properties of the sample through the interaction of light and the electrons in the host sample, x-ray spectroscopy is one of the most powerful tools in modern physics and chemistry.

In solids, electrons can be separated into two categories: core electrons (*inner shell*) and valence electrons (*outer shell*). The valence electrons include the outermost and least bound electrons that are responsible for chemical bonding. Its spatial and energetic separation into occupied and unoccupied states primarily account for the observed physical properties of the material; that is electric, magnetic, thermal, and other properties determined by valence electrons. The core electrons are deeply bound and are almost unchanged to that of free atoms and are well separated in energy and unique to each element. Although generally inert due to their localization near the nucleus of an atom, core electrons provide a method to locally study the valence electronic structure and geometry around a specific atomic site[61].

When an incident photon with sufficient energy interacts with a multi-electron atomic system, an electron can be removed (excited or ionized) from deep electron shells by the photoelectric effect which forms the basis of x-ray absorption spectroscopy (XAS), x-ray photoemission spectroscopy (XPS), and x-ray emission spectroscopy (XES). An electron can absorb a particular energy and is then promoted to a partially filled or empty levels/bands just below a particular ionization threshold, schematically illustrated in Fig. 2.1(a). The perturbation to the ground state involves electrons making transitions into new bound states or unbound continuum states. The character of this excited state depends critically on the energy of the incident radiation. The excited state is unstable, and the system will decay after a certain lifetime via emission of photons (radiative decay) or electrons (non-radiative (Auger) decay) shown in Fig. 2.1(b). Measuring the energy and momentum of the emitted particles allows one to deduce various properties of the system in its ground or excited states.

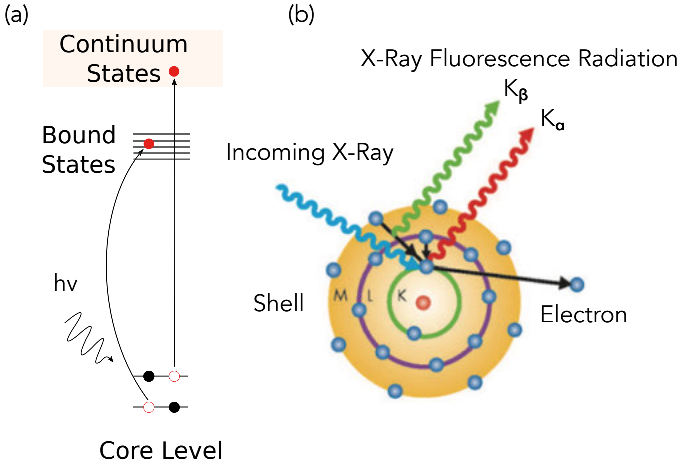

*Figure 2.1* (a) Excitation of a core-electron into either a bound state or a continuum state. (b) The relaxation channels after transition to an excited state.

X-ray spectroscopic techniques can be roughly divided into two types of scattering events, one that is a '*first-order*' scattering event than includes only one photon with incident energy $\hbar\omega_i$, such is the case for XPS and XAS. The core electron is promoted to an empty valence state by an incident x-ray photon of energy. For XPS, we have a photon absorbed and an electron ejected from the sample. These processes are followed by subsequent relaxation process shown schematically in Fig. 2.1(b). For '*second-order*' scattering event, a photon promotes an electron to an excited state and decays radiatively with the emission of an x-ray photon, as is the case for XES and RIXS. There are also three regimes in which x-ray spectroscopy can be divided into based on photon energy: soft x-ray region (~ 20 – 2000 eV), tender x-ray (~ 2000 – 6000 eV), and hard x-ray (~ 6000 – 30000 eV). All three ranges have their own specific qualities as well as offering complimentary information on the overall electronic structure and will be given a brief overview in subsequent sections.

### 2.1.1 Synchrotron Radiation: Tunable Soft & Hard X-rays

In order to perform the many different x-ray spectroscopy experiments, one needs high intensity and high flux tunable x-ray sources. The state-of-the-art instrumentation for these experiments requires synchrotron radiation (SR). When charged particles moving at relativistic speeds along curved trajectories by applied magnetic fields, they emit electromagnetic radiation that is known as synchrotron radiation. This instrument is routinely used throughout the world and provides radiation in a wide spectral range from infrared to hard x-rays. Up to now, three generations of synchrotron radiation sources have been developed, with the fourth generation – called free electron lasers – already in use produces high power and ultrafast pulses of highly coherent radiation. Synchrotron based spectroscopy experiments have become indispensable to study the electronic structure of matter.

### 2.1.2 Storage Rings and Insertion Devices

Figure 2.2 shows the layout of a third generation synchrotron radiation facility, the European Synchrotron Radiation Facility in Grenoble, France. Electrons are projected to relativistic speeds into a well-defined closed circular path called *storage ring* that consists of straight and curved magnetic sections. The energy loss encountered by the electrons from emitted radiation is replenished by an oscillating electric field in a radio frequency cavity. The storage ring consists of alternating curved and long straight sections specifically optimized for producing intense radiation. Several different types of magnetic structures, called *insertion devices*, are tangentially placed to the storage ring to bend the electron beam and emit highly conical beams of light that are delivered to the beamlines.

Common types of insertion devices are the *bending magnet* and the *undulator* and depicted in Fig. 2.2(b) and 2.2(c) respectively. The bending magnet simply bends the electrons in a single curved trajectory, and a narrow cone of radiation with a continuous spectral distribution of is produced (e.g 100 – 1000 eV)[62]. In contrast, the undulator consists of a period array of magnets with alternating polarity of transversal or helical structure. The electrons oscillate in the periodic magnetic structure of the undulator by means of the Lorentz force and coherent x-ray pulses are emitted in a very narrow cone

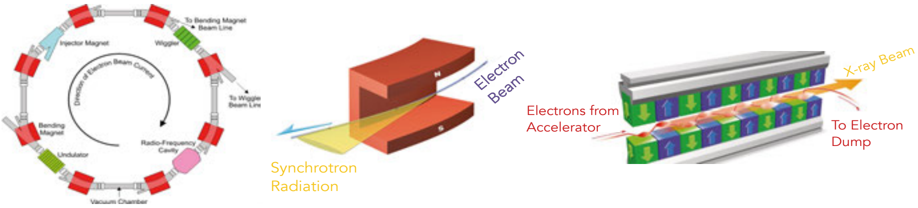

*Figure 2.2* (a) A birds-eye view of a synchrotron radaition ring with different insertion devices. (b). A bending manget . (c). A wiggler (*All figures adapted from* Ref. [62])

with small angular and spectral displacements. The spectral range from an undulator is concentrated into a series of discrete energies (undulator peaks) at which the intensity is greatly enhanced. The desired photon energy is chosen by varying the distance between the gap of the upper and lower magnetic arrays. In order to produce elliptical or circular polarized light, the shifting of magnetic rows in an undulator or a combination of two undulators can produce polarized synchrotron radiation.

### 2.1.3 Beamlines and Endstation

Once the coherent radiation is generated via a bending magnet or an undulator, the light is guided to the experiment in a segment called the *beamline.* A beamline is a series of precision optical elements that direct, monochromatize, and focus the divergent light beam onto the sample, all kept in ultra-high vacuum. The highly monochromatized beam is achieved by diffraction from crystals (hard x-rays) or reflection gratings (soft x-rays) through different slits and mirrors. The optical components are general to most beamlines, but also vary depending on the type of experiment conducted. The most common design in the soft x-ray range is using a spherical grazing monochromator (SGM) at grazing incidence. The divergent incoming beam is diffracted and focuses the desired photon energy onto the exit slit of the monochromator. The highly monochromatized beam is further focused with a refocusing mirror to guide the light onto the sample surface. For hard x-rays, monochromatization happens with high-quality Bragg crystals suited for a specific photon energy range.

# 2.2 Principles of Photoemission Spectroscopy (PES)

## 2.2.1 General Formalism: The Photoemission Process

Figure 2.3 illustrates a schematic on the principle of the photoemission process, which is based on the photoelectric effect. When a photon with sufficient energy $hv$ is illuminated on a solid, there is a probability that a bound electron is excited or released from the sample. The kinetic energy of the released photoelectron can be described as the difference between the initial ground state of the neutral atom and the final excited state of the ionized atom as:

$$E_{final} - E_{initial} = E_{K.E.} = hv - E_{B.E.} - \phi \quad (2.1)$$

where $E_{\mathrm{K.E.}}$ is measured from the vacuum level, and $\phi$ is the work of function of the sample, and $E_{\mathrm{B.E.}}$ is the binding energy measured from the Fermi level ($E_{\mathrm{F}}$). Therefore, the characteristic binding energy of a core electron is determined by the incident photon minus the measured kinetic energy of the outgoing photoelectron. Since the core-level is characteristic to each element, XPS is useful for the elemental analysis in solids. Any deviation of the binding energy (B.E) of a core-electron from that of a free atom provides valuable information on chemical bonding of valence electrons. An electrostatic hemispherical analyzer measures the kinetic energy, and the work function is set by the spectrometer that is electrically connected to the sample. The energy of the incoming light ($hv_i$) is known from an x-ray source that is either determined by the anode material or from a tunable source such

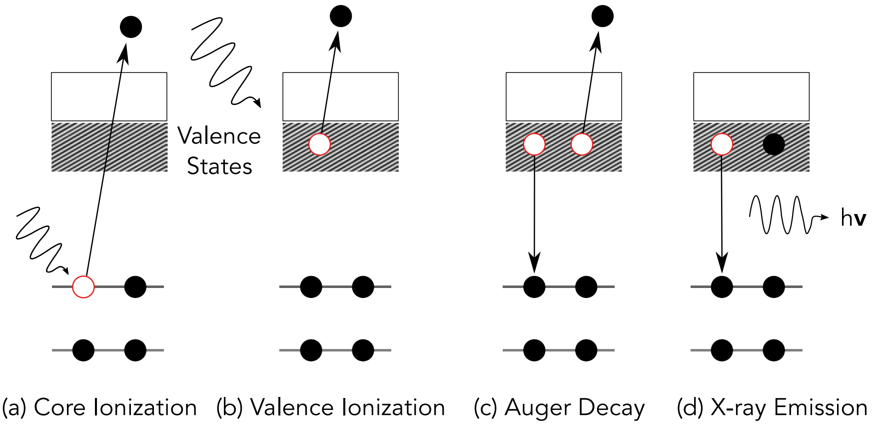

*Figure 2.3* Ionization process of a (a) core electron and (b) and valence electron at different incident energies. (c) Auger decay mechanism, and (d) radiative decay with the emission of a photon after an absorption event.

as a synchrotron. The core principle is the identification and speciation of each photoemission process that can be identified to a specific atom.

After a core-hole is created, the excited state will decay rapidly by a transition of an electron from higher lying shell to fill the core hole. This decay process, a recombination of an electron with a core hole can either be non-radiative, i.e. Auger electron decay (Fig. 2.3(c)), or radiatively by an x-ray photon (*see* Fig. 2.3(d)). Since the core-hole is often characteristic to a specific element, the energy of the decay transitions (Auger electron or x-ray emission) can also be separated and identified. An Auger electron has a characteristic energy, distinguishable from a normal photoelectron, and is a commonly used spectroscopic tool.

The transition probability $\omega$ between two states, one that is described in terms of transition from initial ground state $\Psi_\mathrm{i}$ to final state $\Psi_\mathrm{f}$ is given by Fermi's Golden Rule:

$$\omega = \frac{2\pi}{\hbar}\left|\langle\Psi_f|H|\Psi_i\rangle\right|^2\delta\left(E_f - E_i - hv\right) \qquad (2.2)$$

The delta function (δ) ensures the conservation of energy. The perturbation operator H, the interaction Hamiltonian that causes the transition, is expressed as:

$$H = \frac{e}{2m_e c}(\boldsymbol{A}\cdot\boldsymbol{p} + \boldsymbol{p}\cdot\boldsymbol{A}) - e\Phi + \frac{e^2}{2m_e c^2}|\boldsymbol{A}^2| \qquad (2.3)$$

where $m_e$ is the electron mass, $e$ is the electronic charge, and $c$ the speed of light. **A** is the vector potential operation and Φ is the scalar potential of the exciting electromagnetic field. **p** is the momentum operator of the electron. This first order optical process, described by the first term and a first order perturbation is a suitable description of a photoemission process. The second term can be neglected as it describes a two-phonon process.

During the photoemission process and the creation of a core hole, the surrounding electron cloud of the remaining ion contracts (relaxes) in order to screen the positive charge. The subsequent relaxation may lead to the so-called shake-up and/or shake-off process, which are also observed in the photoemission spectra.

### 2.2.2 Electron Escape Depth and Photoionization

After the local absorption of a photon, the photoelectron must propagate through the sample to the surface. In route to the surface, the excited photoelectron suffers energy losses through interactions with other electrons or collective motions in the surrounding medium. The magnitude and energy dependence on the mean free path, $\lambda$, is dependent on the scattering mechanism in the samples. This important parameter reflects the mean distance between two inelastic collision of the photoelectron, which is a material and photon energy dependent parameter. The escape depth for all materials roughly follows a "universal curve" as a function of incident energy shown in Fig. 2.4. For soft x-rays, the photoelectron ranges will be in the order of 5-10 Å, which makes the soft x-ray range more surface sensitive, and hard x-rays more bulk sensitive.

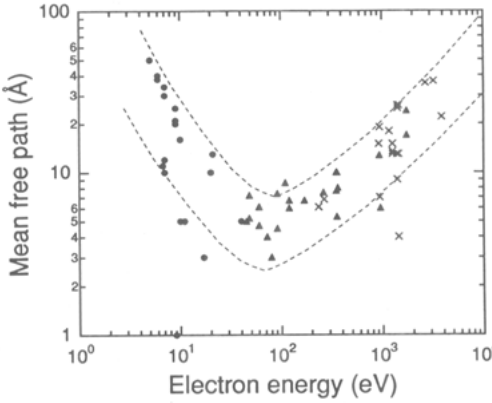

*Figure 2.4* Inelastic mean free path of electrons as a function of electron kinetic energy.

### 2.2.3 Resonant Photoemission Spectroscopy

When the incident photon energy is tuned near the ionization energy of a core hole, the emission from this resonant state is substantially modulated. This enhancement of is due to an interference of the core-hole and direct valence band photoemission. This phenomena leads to a pronounced effects for strongly interacting electrons systems where there is a giant enhancement in the photoemission cross section at resonance. This feature is most significant in systems that contain partially occupied *d* shells that results in strong Coulombic interactions among valence electrons. For example, when the incident photon energy is equal to the energy difference between the *p* core level and the valence $d$ states, a direct photoemission process of a valence $d$ electron occurs as:

$$p^6d^N + hv \rightarrow p^6d^{N-1} + e^-,$$

The resonant process includes another intermediate step and is expressed as:

$$p^6d^N + hv \rightarrow p^5d^{N+1} \rightarrow p^6d^{N-1} + e^-.$$

Both the initial and final states of two processes have the same electron configurations. A quantum-mechanical interference occurs between the valence photoemission and core-hole excitation with Auger decay and thus a substantial change in measured intensity. The electron emission is via an Auger-type path, where a photon excites the system into an intermediate state with a core hole, and the core hole decays via Coulomb interactions in an Auger-like autoionization process. This leads to two new possibilities for the electron spectra. One channel is characterized by involving the bound state photoelectron, thus called *participator decay*, and the other channel with an electron in the normally unoccupied levels in the final state with two electrons removed in an Auger-like transition termed *spectator decay*. An important distinction is the constant kinetic energy for the participator decay, whereas spectator decay shift in binding energy as the photon energy is scanned across an absorption edge. A schematic illustration of the resonant photoemission process via the absorption process is depicted in Fig. 2.5. Since the enhancement takes place only for the emission of $d$ electrons, one can obtain the $d$ partial spectral density weight of the valence band[63]. This technique is extensively used in this thesis, particularly for work on bulk and thin film oxides discussed in Chapter 3 and 4.

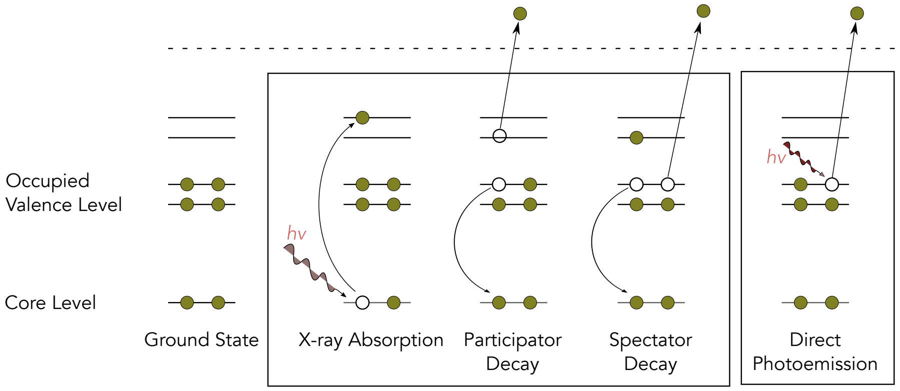

*Figure 2.5* Schematic illustration of the resonant photoemission process, in which a core electron is excited to a resonant unoccupied state, and the subsequent decay results in a final state the same as direct photoemission.

## 2.3 Principles of X-Ray Absorption and Emission Spectroscopy

The absorption and emission of x-rays in condensed or soft matter is rich in phenomena and offer a breadth of quantitative analysis. The impact of XAS and XES on a variety of scientific disciplines has offered new insights that are supported by different levels of theory, much of it in the last few decades. The significant accomplishments are possible with advancements in x-ray optics, detectors and analyzers, as well as the availability of high-brilliance beamlines. These observations have pushed the field of condensed and soft matter physics to new heights.

### 2.3.1 Introduction to XAS and HERFD-XAS

As with other inner-shell spectroscopies, x-ray absorption (XAS) involves the excitation of a core-level electron to unoccupied states of a solid as shown in Fig. 2.6(a). The energy of the incoming photon is of the same order as the binding energy of a core electron. As a result, the excited core electrons are a reflection of the mass absorption coefficient ($\mu$) of a particular shell and an approximate symmetry-projected unoccupied density of states of the excited state, as shown in Fig. 2.6(b). The region before and after the absorption edge characterized by transition of the photoelectron to unoccupied bound states is called x-ray near edge structure (XANES). Furthermore, XANES absorption features are sensitive to local symmetry, oxidation state, and local site geometry of the transition metal ion. In the extended region of the absorption spectrum, a region fittingly named extended x-ray absorption find structure (EXAFS), the excited electron has significant kinetic energy and yields extensive quantitative analysis on the local geometry such as bond lengths, coordination, etc[61].

Like XPS, XAS is a *first-order* optical process with its cross-section described by the Fermi Golden Rule stated in Equation 2.2. XAS spectra are usually measured indirectly by measuring the secondary process since it is much easier to perform experimentally. Highly excited core-hole states are relaxed by a variety of mechanisms, the two most significant being emission of an Auger electron and x-ray fluorescence. The absorption can be measured indirectly by detecting the Auger electrons or, more commonly, by detecting electrons from multiple secondary processes called total electron yield (TEY). For conducting samples, this can also be done by measuring the drain current of the sample. The radiative relaxation is recorded in the form of a total fluorescence yield (TFY), the summed fluorescence yields of all dipole-allowed transitions to fill the core-hole. Much of the information obtained from TEY and TFY techniques yield the same absorption spectrum, however differ in their sensitivity to bulk and surface information. The escape depth of photoelectrons is rather shallow (~ 50 Å) and limits the information to the top-most layers of the surface, thus restricting TEY method for surface sensitive studies. Fluorescence emission comes from deep within the bulk of the samples, where the escape depth of the fluorescent photons is on the same order as the penetration depth, i.e. of ~ 1000 Å. Therefore, this technique is very suitable for bulk properties and buried layers. The major drawback of this technique is the saturation and self-absorption effects that deviate from a linear relation to the absorption coefficient. These effects are mitigated by changing the experimental geometry to grazing incidence as well as quantitate correction using reference compounds. Recently, an alternative method was developed in order to measure an absorption spectrum based on the integrated x-ray emission from a different element in the sample[64], termed inverse partial fluorescence yield (IPFY). IPFY is linearly proportional to the x-ray absorption cross-section without any corrections due to saturation or self-absorption effects[65].

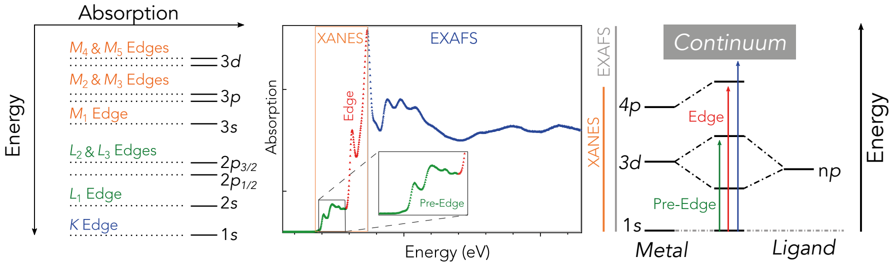

*Figure 2.6* (a) The absorption transition resulting in the excitation of a core electron. (b) The different regions of the x-ray absorption spectrum that bear unique information as a function of incident energy. (c) The characteristic regions in typical x-ray absorption spectra.

There are two characteristic features in the edge region of a XANES spectrum: 1) an intense absorption edge, and 2) a weak pre-edge feature seen just before the onset of the main absorption line as illustrated in Fig. 2.6(b). For 3*d* transition metals, the intense features from dipole allowed transition give information related to the oxidation state of the ion, whereas the pre-edge feature provide additional information on the symmetry of the system[66]. This region is particularly suitable for systems that have a loss of inversion symmetry, such as ferroelectrics. Also the energy position, intensity, and the number of pre-edge peaks also provide information on oxidation state, covalency, and coordination number[61].

A relative new technique that also indirectly measures the x-ray absorption of a particular shell with substantial improvement in resolution is high-energy fluorescence detected XAS, or HERFD-XAS[67,68]. In this scheme, one

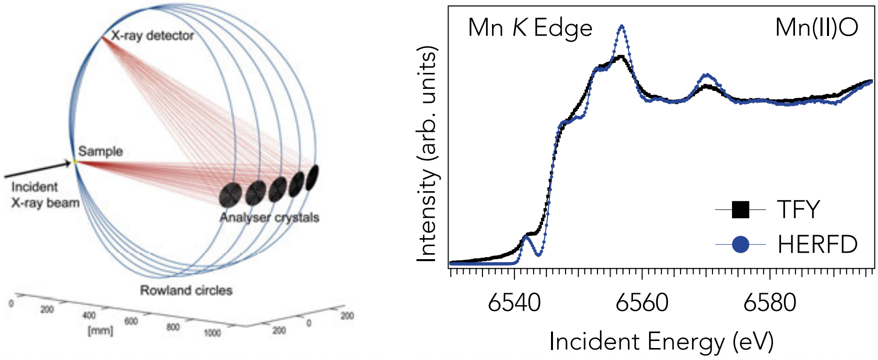

*Figure 2.7* – Illustration of an energy-dispersive spectrometer in a Johansson geometry used for HERFD-XAS technique (*Figure adapted from* Ref. [67]). (b) Comparison between total fluorescence yield (TFY, black) and high-energy resolution fluorescence detected x-ray absorption (HERFD-XAS) spectra of MnO at the Mn *K* absorption edge.

is able to detect emission form a single dominant decay channel, i.e. the $K_\alpha$ line of a selected element's absorption edge, thus making this a partial fluorescence yield technique. The intensity variation of the tuned fluorescence line is scanned across an absorption edge. This secondary process detection is realized with a wavelength dispersive instrument to discriminate between various decay channels, e.g. only the $K_\alpha$ fluorescence lines. The data acquisition principle is shown in Fig. 2.7 (*left*) for the example of a scanning Johann type spectrometer. This fluorescence detected XAS is a second order optical (photon-in/photon-out) process that is theoretically described by the Kramers-Heisenberg equation (*see next section*). The lifetime of the final state core-hole governs the overall resolution of the spectra, in the HERFD-XAS case, is the core-hole state of the decaying emission line. This detection scheme has the tremendous advantages offering high single-to-background round ratio and improved resolution. The broadening is reduced to the core-hole state of the recorded emission line rather than the core-hole of the excited photoelectron, as demonstrated in the spectrum shape in Fig. 2.7 (*right*).

## 2.2.2 X-Ray Emission Spectroscopy

Following an absorption event, the excited atom is left with a core-hole that relaxes through radiative (photons) and non-radiative channels (electrons). The emitted energy of the x-ray photon is the difference the energized core-state ($E_i$) and a higher final state ($E_f$). The intermediate state of non-resonant x-ray emission exhibits a continuum electron, in the photoelectron state $|\phi_\epsilon\rangle$ with energy $\epsilon$. The recorded fluorescence spans a broad energy range and dominated by the dipole selection rules: $\Delta l = \pm 1$ and $\Delta j = \pm 1$ and expressed by the Kramers-Heisenberg relation[69] (Equation 2.4). This formalism holds

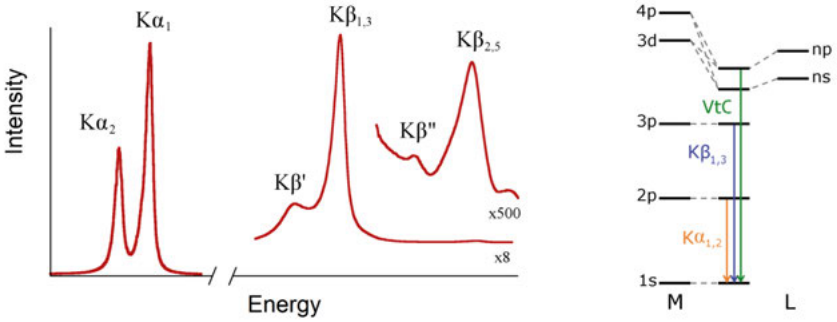

*Figure 2.8* – X-ray emission spectrum marked with $K_{\alpha}$ and $K_{\beta}$ core-to-core emission lines along with satellite Valence-to-Core ($K_{\beta 2,5}$ and $K_{\beta''}$) emission lines (*left*). A schematic that depicts the transitions recorded in an XES spectrum (*right*).

if one assumes the incident photon energy Γ is well above the x-ray absorption threshold.  The intensity of the emitted energy covers a broad range of fluorescence lines and satellite states as shown in Fig. 2.8. The process therefore shows little dependence on the energy that is used for the initial photoionization process. The subsequent decay directly maps the local occupied partial density of states due to the atomic character of the core levels and the dipole selection rules. This information is complementary to the unoccupied partial sates of an XAS spectrum, as both provide information on local electronic structure and symmetry of the absorbing atom.

X-ray emission spectra are often divided into two main energy regimes that require altogether different instrumentation: soft x-rays (<1500 eV) and hard x-rays (> 3 keV). They are also characterized between lower in energy core-to-core transitions (CtC-XES) and weak and sensitive valence-to-core transition (VtC-XES), as show in Fig. 2.8 for a complete collection of a *K* edge emission. The main transition fluorescence transitions, mainly $K_{\alpha}$ and $K_{\beta}$ transitions, shown on the lower energy side in Fig. 2.8, bears information on symmetry, local spin density, and indirectly the valence shell electron configuration. The VtC peaks, exceedingly weak and higher in energy, probes the valence levels of the system and provides complementary information to photoemission spectroscopy due to the element-specific probe[70].

In the present work, the absorption and emission of *K* and *L* edges are probed for TM cations and halide anions. The subsequent decay of fluorescence lines from shallow levels and valence levels are monitored to interpret the partial valence states and local structure.

### 2.2.3 Resonant Inelastic X-Ray Scattering

RIXS is a photon-in/photon-out technique that maps the energy and momentum transferred to a system. The changes in energy, momentum, and polarization of the scattered photons are transferred to intrinsic excitations of the material under study, which are then detected via the RIXS process. Using conservation laws and selection rules, one can determine the dispersion relations between separate excitations in the sample. Common to many transition metal oxides and their archetypes, a range of excitations such as charge, orbital, spin, lattice, and even coupled ones are observed in the acquired spectra[71–74]. Much of the advancement in RIXS has benefitted from high-flux synchrotron sources and remarkable high-resolution instrumentation such as beamline monochromators and spectrometers.

In order to derive the basic formula describing the RIXS process, let us consider an x-ray scattering process that involves a photon with energy $h\nu_{in}$ incident on a material that then decays radiatively with photon energy $h\nu_{\mathrm{out}}$. The perturbation to the Hamiltonian of the photo-excited electron accounts for a first-order and second-order terms that define the scattering cross-section. This transition probability from the ground state to a final state induced by the two Hamiltonian terms, by virtue of the Fermi's golden rule, produces a second-order process that requires an intermediate state before de-excitation. This combined excitation and de-excitation process that is coherently correlated by the Kramers-Heisenberg equation:

$$F(\Omega,\omega) = \sum_f \left| \sum_m \frac{\langle f|T|m\rangle\langle m|T|i\rangle}{E_i + \Omega - E_m + m\Gamma_m} \right|^2 + \delta(E_i + \Omega - E_f - \omega) \qquad (2.4)$$

where $|i>$ and $|m>$ represent the initial and intermediate states with energies $E_i$ and $E_m$ respectively, while $|f>$ and $E_f$ correspond to the final state configuration and energy. The transfer operator is T and broadening of the overall spectra is denoted by $\Gamma_m$, the intermediate state of the second-order process. RIXS implies choosing the excitation energy, usually close to a characteristic absorption edge of an element, where the cross section in Eq. 2.4 changes dramatically and gives rise to additional features than non-resonant XES. Several different channels can emerge at different incident x-ray energies. Correspondingly, the overall RIXS spectra contain both signatures of photons emitted elastically, *i.e.* with the same energy as that of incident photons, and with inelastic photons, for which the emitted x-ray energy has changed. Overall, the scattering process leaves the system in a charge-neutral but excited state.

Figure 2.9(a) visualizes the RIXS process by an energy level diagram that is conceptually separated into two steps. The first process involves an excitation of a core electron to an unoccupied band, and subsequent decay of an occupied valence electron. The indirect RIXS creates a scattering of the localized core-hole wave of the photoelectron with the valence electrons, leaving behind a range of excitations in the valence electrons mentioned previously. The features of these excitations take shape on an energy loss spectrum that is a measure of energy transferred to the sample. The elastic line is the zero energy loss to system ($E_{in} - E_{out} = 0$) and is common to almost all RIXS spectra and varies in intensity at different absorption edges. The inelastic peaks are more interesting, as they provide clues into the interactions between the different quantum parameters of the system.

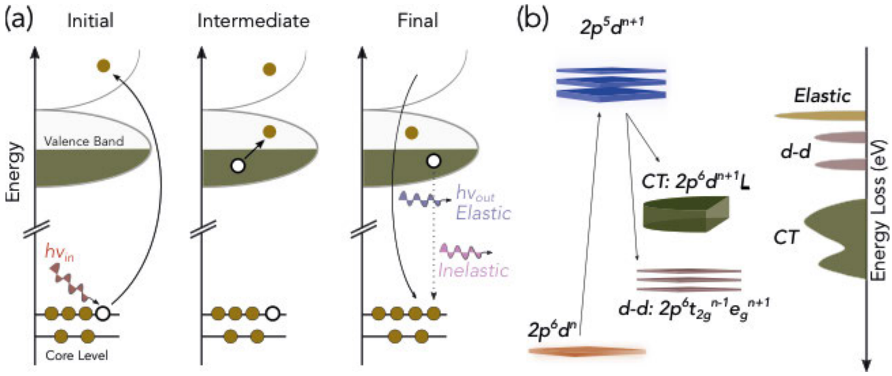

*Figure 2.9* (a) Schematic view of the RIXS process. (b) Illustration of a $2p \rightarrow 3d$ RIXS process that probes two finals states: a charge-transfer from O $2p \rightarrow$ TM $3d$ and/or excitations within the *d* manifold.

The characteristic traits of RIXS features are highlighted in this section. In general, the entirety range of features – both elastic and inelastic is strongly dependent on the photon energy, geometry of the experiment, and the material system. The RIXS experiments performed in this thesis are on transition metal oxides at Ti *K*, Mn *K*, Fe *L,* and O *K* edges, and at I $L_1$ edge for the halide perovskite compounds, covering both soft (100 – 2000 eV) and hard x-ray (E > 2000 eV) edges. The separate excitations that are probed in this thesis are charge transfer (CT) and *d-d* excitations. Charge-transfer excitation covers an energy range between 4-10 eV in energy loss ($hv_{out} - hv_{in}$) that are typically observed for transition metal compounds due to the broad band hybridization between the metal *d* and ligand *p* states. Assuming that the system is excited to a $d^{N+1}$ condition, this results in a $d^{N+1}\underline{L}$ intermediate state where $\underline{L}$ is the core-hole in the ligand. This feature is obtained when the de-excitation process leaves behind an electron the TM *d* orbital with a hole in the $\underline{L}$ valance band, and reflects the O $2p$ – M $3d$ hybridization.

The *d* orbitals are directly probed at the *L* edge in RIXS experiments. The *d*-*d* excitation is in the range of 1-3 eV energy loss which correspond to electron-hole transition between the ligand-field non-degenerate *d* states. This transition is generally forbidden due to the dipole selection rules, however are observed due to the coherent second-order nature of the RIXS process. Once a *d* orbital is reached from an excitation of the *L* edge, the intermediate state is an excited electron that is strongly bound to the core hole that does not easily delocalize to neighboring sites. The subsequent de-excitation is the decays from a different *d* orbital filling the core-hole so that the number of electrons in the system is preserved. This excitation is especially strong in transition-metal oxides which manifest strong correlations. The excitation process leaves a change in the occupancy of the *d* orbitals that is largely determined by the crystal field splitting.

## 2.4 Thin Film Fabrication of Ferroelectrics

### 2.4.1 Pulsed Laser Deposition

Perovskite oxides have a simple crystalline structure that permits the epitaxial growth onto single crystalline substrates. The primary technique to grow oxide thin films is pulsed laser deposition (PLD) technique. This technique allows fabrication of thin films using stoichiometric targets of the same compound for growth and is relatively simple from the application context. In reality, the interaction of the laser-matter interaction and the subsequent generation of plasma is dynamic and very complex and not entirely understood[75].

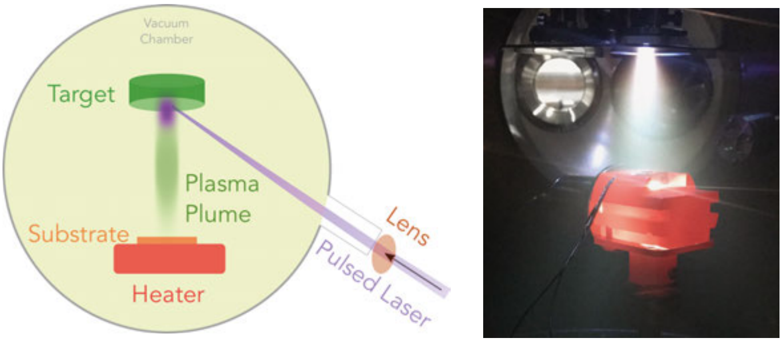

*Figure 2.10* A schematic illustration of the PLD deposition process (*left*). A plasma plume produced from a $BaTiO_3$ target immediately after ablated by a 248 nm KrF laser (*right*).

PLD is a physical deposition technique in which an intense laser ablates and vaporizes the target material to form onto a single crystalline substrate. The stoichiometric transfer is ensured as long as the ablation is homogenous. The laser used for this thesis is a UV high-power pulsed laser based on an excimer KrF (248 nm). The principles of operation are: 1) the incoming laser vaporizes the target material, 2) the generation of a plasma that expands rapidly and dynamically interacts with the background gas, and 3) nucleation of a solid phase from a supersaturated gas that reproduce the target composition onto a substrate. The desired nucleation of the material onto the substrate can be adjusted by a number of independent parameters. These include the target-substrate distance, the laser energy density and repetition rate, the oxygen partial pressure, and the temperature of the substrate. The nucleation of the target material constituents on a sample surface determines the growth mode of the film: island growth (Volmer-Weber), layer-by-later (Frank-Van der Merwe), or Stranski-Krastanov growth[76].

Results on thin film deposition are reported in Chapter 4 of this thesis.

### 2.4.2 X-ray Diffraction and Reflectivity

X-ray diffraction experiments were performed on a PanAlytical X'Pert four axes diffractometer. This setup is equipped with a Cu $K_\alpha$ x-ray tube with a wavelength of 1.5406 Å and x-rays emitted onto the sample with a parallel beam configuration, both for x-ray reflectivity and out-of-plane diffraction measurements. The two separate measurements were used to obtain out-of-plane lattice parameters, understanding of the crystalline and epitaxial quality, and thickness of the films. For x-ray diffraction measurements, a PiXel detector was used and a proportional detector consisting of a xenon/methane mixture for XRR measurements.

### 2.4.3 Piezoforce Microscopy

Scanning probe microscopy is used to provide information on the surface morphology of deposited thin films. Atomic force microscopy (AFM) and the more advanced piezoresponse atomic force microscopy (PFM) have become reliable tools to study ferroelectric thin films[77]. In the AFM technique, a small tip is brought to the proximity of the film surface and the deformation of sample surface is monitored. A collimated laser beam reflects the cantilever of the AFM probe and is reflected to a photodetector to image the sample surface. The image can provide clues to the sample roughness, homogeneity, and type of film growth.

Piezoresponse is an extended type of force microscopy that measures the dynamic electromechanical response of a ferroelectric sample. Ferroelectricity is commonly demonstrated by the PFM hysteresis loops and a phase difference of the acquired images before and after poling[78–80]. The technique involves the application of an AC voltage to the conducting tip in mechanical contact with the surface and the subsequent oscillation of the tip is detected by a lock-in technique. Due to the inverse piezoelectric effect, the ferroelectric material responds with an expansion or contraction, which is measured as the cantilever deflects through a laser spot. During PFM measurements, the measured amplitude and phase of the deflected signal contains information about the local ferroelectric strength and the orientation of the ferroelectric domain. The PFM signal yields local hysteresis loops and the switching voltage and can be extracted.

Results on the ferroelectric properties of BTO and doped BTO thin films are presented in Chapter 5.

# 3 Bulk Perovskite Oxides

In this section we review the work done on two bulk perovskite oxides: Mo doped $LaFeO_3$ and $Sr_2FeMoO_6$. The electron doped $LaFe_{1-x}Mo_xO_3$ (LFMO) exhibits a novel ground state that combines room temperature metallicity with antiferromagnetic ordering[81]. The second compound, $Sr_2FeMoO_6$ (SFMO) has received considerable attention since the discovery of a tunneling magnetoresistance (MR) and spin-polarized metallicity at room temperature[82]. A combination of x-ray spectroscopies is used to study the valence electronic structure.

Both these materials offer an attractive possibility for their use in magnetic devices and spintronics[83,84], which is the intention of our future work. The motivation for this work here is to comprehend the electronic structure through different x-ray techniques and reveal the conditions that make two materials appealing for spintronic applications.

## 3.1 Insulator-to-Metallic Antiferromagnetic Oxide: $LaFe_{1-x}Mo_xO_3$

In Paper I, we report on a new material that exhibits a rare ground state in a perovskite oxide. By doping at the B-site of the $LaFeO_3$ oxide with the 4*d* Mo transition metal ($LaFe_{1-x}Mo_xO_3$), the system undergoes a gradual crossover from an insulating to metallic state at room temperature while retaining its antiferromagnetic (AFM) spin ordering. This new compound was investigated through several laboratory and synchrotron-based techniques to show its unique ground state properties. This material may hold promise in its use in antiferromagnetic spintronics, as well as fundamental questions in regards to its unusual coexistence of metallicity and AFM at room temperature.

Six samples of $LaFe_{1-x}Mo_xO_3$ (LFMO) with Mo doping at $x = 0.00$, 0.05, 0.10, 0.15, 0.20, 0.25 were synthesized by the solid-state route. Magnetic measurements were carried out using a Quantum Design SQUID magnetometer, as shown in Fig. 3.1(a). The AFM transition Neel temperature ($T_N$) for the doped compounds decrease linearly with increased Mo doping (see *inset* of Fig. 3.1(a)). This indicates that even at high doping concentration, the

AFM order is still maintained. Changes in resistivity should also accompany this gradual metallic transition and has been measured using a four-point probe setup as shown in Fig. 3.1(b). There is a substantial decrease in the resistivity magnitude for LFMO-0.25 compared to LFMO-0.10, which remains insulating. Although the slope negative slope suggests an insulating behavior (a negative $\partial\rho/\partial t$), it does not diverge and saturates at low temperatures. This resistivity is attributed to the formation of an insulating Mo$^{6+}$ that exists at the grain boundaries, as shown by several previous studies and is a common observation in polycrystalline ceramics[82,85]. This is further investigated through scanning tunneling microscopy (STS) measurements shown in Fig 3.1(c). A finite $dI/dV$ at zero bias ($V = 0$) exists for both 20% and 25% Mo doping, indicating a finite DOS at $E_F$ for both samples, which is insignificant for $x = 0.0$, 0.10, and 0.15 at $V = 0$. The effect of surface treatment is resolved for the metallic LFMO-0.20 sample, where the untreated sample revealed negligible $dI/dV$ intensity (see *inset* Fig. 3.1(c)) compared against the *in-situ* cleaned LFMO-0.20 sample. This data set corroborates with the measured photoemission spectra and confirms the crossover to metallic state through electron doping.

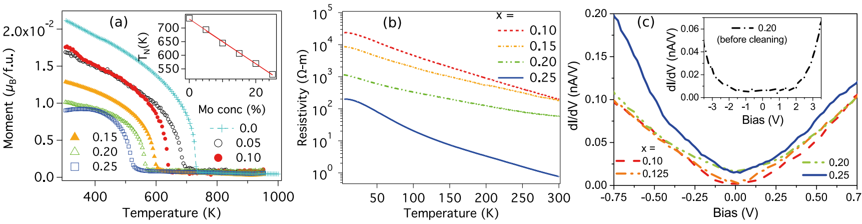

*Figure 3.1* (a) Temperature dependence on magnetization for all compositions. (b) The resistivity vs. temperature plots and (c) Scanning tunneling spectroscopy (STS) plots on the Mo doped samples. The inset compares the STS for an untreated $x = 0.20$ sample.

The mechanism proposed for the electronic insulator-to-metallic transition can be contended to the mixed-valency in the Fe ions and concurrent structural distortions. In the pure LaFeO$_3$, the ground state ionic picture for Fe is a Fe$^{3+}$ ion that is localized and positioned equidistantly from its' six adjacent oxygen atoms. The mixed valency is probed through Fe $L$ x-ray absorption spectroscopy shown in Fig. 3.2(a) for all samples. As evidenced from the fitted data for $x = 0.20$ spectra in Fig. 3.2(b), the lower energy peak is predominantly Fe$^{2+}$ while the peak at higher photon energy is attributed to Fe$^{3+}$. The Fe$^{2+}$ component monotonically accrues as the Mo doping concentration steadily increases.

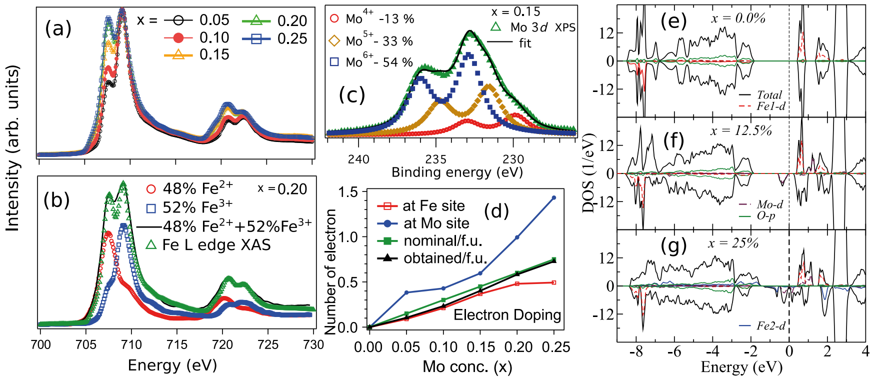

*Figure 3.2* (a) Fe *L* edge XAS spectra for all compositions that are *in-situ* scraped with a diamond file. (b) Fitted data for $x$ = 0.20 sample by the weighted average in terms of $Fe^{2+}$ and $Fe^{3+}$. (c) Mo 3*d* core level XPS spectra for $x$ = 0.15. (d) Different contributions of doped electrons obtained at Fe band, Mo band, and the total/f.u. and nominal/f.u. (e)-(g) Optimized GGA+U total and partial density of states showing the two charge disproportionated Fe sites.

To assess the changes to Mo valency, PES was used to probe the Mo 3*d* core level, as shown for LFMO-0.15 in Fig 3.2(c). The spectrum is fitted considering different Mo oxidation states and a satisfactory fit only with three Mo components ($Mo^{4+}$, $Mo^{5+}$, and $Mo^{6+}$) to match the experimental spectra. The average valency for both Fe and Mo ions is extracted for all samples using these two core-level spectra. The obtained numbers of doped electrons at the Fe and Mo sites relative to their most stable valency of 3+ and 6+ respectively, are plotted in Fig. 3.2(d). With increasing doping concentration, electrons gradually fill both Fe and Mo bands. However, the electron doping rate at the Fe sites reduce after $x$ = 0.15 and saturates to ~0.5$e^-$/f.u. for $x \geq 0.20$. Further inclusion of Mo ions to the system, i.e. as for the case of the $x$ = 0.25 sample, pushes all additional charge to the Mo sites, as evident from the identical spectra for $x$ = 0.20 and $x$ = 0.25 in Fe 2*p* XAS in Fig. 3.2(a). These observations imply that the electron doping at the Fe sites reaches a threshold when the valency becomes 2.5+ exceeding 20% Mo doping. It can be implied that the 2.5+ average valency forces an equal sharing of one electron between two Fe-sites. From our theoretical work (*see* Fig. 3.2(e) - (g)), the Fe states are found to be insulating and localized, which also suggest an equal number of $Fe^{3+}$ and $Fe^{2+}$ ions in the system for $x$ = 0.25. This provides further evidence for a charge disproportionation in this system where itinerant and localized orbitals reside on different atomic sties.

## 3.2 Valence Electronic Structure of $LaFe_{1-x}Mo_xO_3$

The results on the valence electronic structure for Mo-doped $LaFe_{1-x}Mo_xO_3$ are taken from a working manuscript (Paper II). The purpose of this study is to combine several x-ray spectroscopies to resolve the ground state electronic structure and connect the concomitant structural distortions as a function of doping.

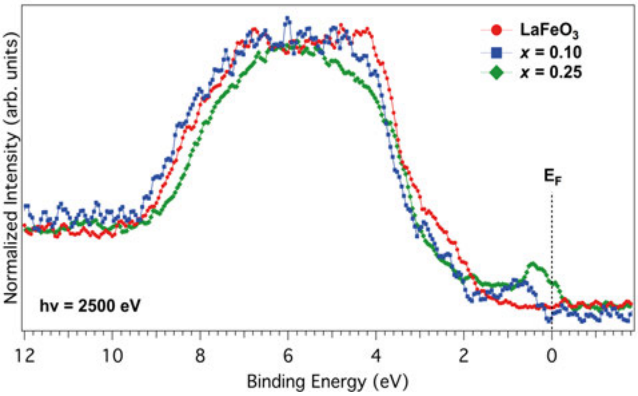

*Figure 3.3* HAXPES data measured at 2500 eV on the $LaFe_{1-x}Mo_xO_3$ series. The insulating $LaFeO_3$ and $x = 0.10$ compounds exhibits a gap between the valence band maximum and the Fermi level ($E_F$), whereas for the $x = 0.25$ composition, there is clear density of states at $E_F$, characteristic of a metal.

Figure 3.3 shows the experimental valence band as measured by photoelectron spectroscopy measured at an incident energy of 2500 eV for $LaFe_{1-x}Mo_xO_3$ compounds ($x = 0.0$, 0.10, and 0.25). A closer inspection of the valence band near the Fermi level ($E_F$) shows an increase in spectral weight as Mo content is increased. For the parent compound $LaFeO_3$, a sizable gap between the valence band maximum (VBM) and the Fermi level ($E_F$), in agreement with a previous soft x-ray study on $LaFeO_3$[86,87]. For $x = 0.10$ doped sample, a nominal increase in states appear at 1 eV in binding energy (B.E.), however it is negligible at 0 eV, consistent with its insulating properties. Conversely, for the $x = 0.25$ sample, we observe a sizeable intensity across $E_F$, confirming the transition from an insulating $LaFeO_3$ to a metallic state by sufficient doping at the B site[81].

A more comprehensive study on the valence electronic structure has been probed through resonant photoelectron spectroscopy at the Mo $L_3$ and Fe $L_3$ edges. The element-selective projection to the partial density of states (DOS) through RPES spectra allow for identification to which TM states constitute the valence band and the extent of their energy positions and hybridization.

Fig. 3.4(b) shows RPES spectrum collected at range of incident energies across the Mo $L_3$ absorption edge (Fig. 3.4(a)). Three structures are enhanced when the energy approaches the absorption maximum. The spectral region around 0 eV B.E. shows an intense and narrow peak (peak labeled A) that can be assigned to Mo $t_{2g}$ states[81], where the itinerant electrons in the partially filled sub-band gives rise to the metallicity for $x = 0.25$. The broad enhancement in the 5-8 eV range signals Mo 4*d* - O 2*p* admixture as was shown by our band structure calculations in the previous study[81]. These spectra qualitatively show the emergence of new Mo 4*d* states that establish the metallicity in this material for doping levels at $x = 0.25$.

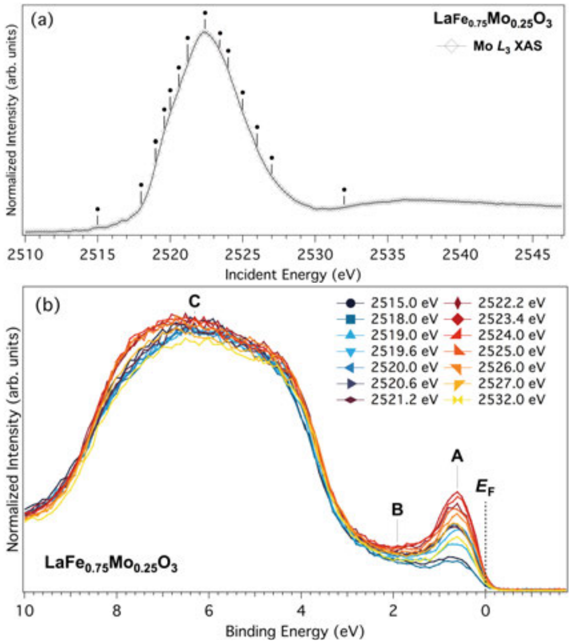

*Figure 3.4* (a) Mo $L_3$ absorption spectrum for LFMO-0.25 measured in TEY mode. The tick marks indicate the excitation energies used to collect photoemission spectra. (b) RPES spectra for $LaFe_{0.75}Mo_{0.25}O_3$ showing three enhanced spectral features that relate to Mo 4*d* contribution in the valence band.

The RPES spectrum collected across the Fe $L_3$ absorption edge is shown in Fig. 3.5. The resonant spectra show four principal structures that are enhanced as the excitation energy is tuned to the resonance condition (709. 0 eV). The intensity around $E_F$ shows no enhancements at the absorption maximum, indicating that the states at $E_F$ have no contributions from Fe, but are solely due to Mo 4*d* states, as discussed in the previous section and corroborated by band structure calculations[81]. The inset in Fig 3.5(b) shows a narrow range of the valence band expanded at a few selected energies (703.0, 707.5, 709.0, and well above resonance at 712.1 eV). When the incident energy is tuned to the maximum of the shoulder peak, associated with $Fe^{2+}$ species, an enhancement for states just below the $E_F$ is observed (*see* peak D). Conversely, at the absorption maximum spectrum (709.0 eV), the structure E near 3 eV in binding energy gains substantial intensity in contrast to the off-resonance energy (703.3 eV) - with much more than at excitation energy corresponding to the peak representative of $Fe^{2+}$. These two structures may point to spectral weight emerging from the two inequivalent Fe sites, i.e. the local charge disproportionation of Fe in the metallic compound.

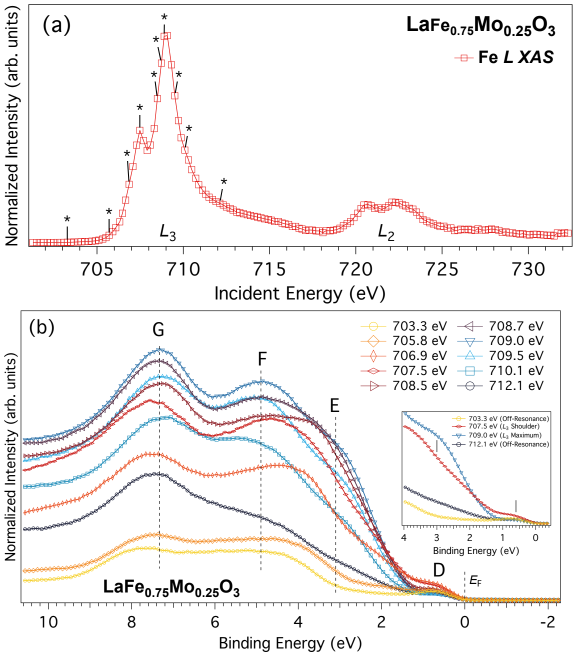

*Figure 3.5* (a) The Fe $L_{2,3}$ XAS spectrum for $x$ = 0.25 with a strong shoulder centered at ~ 707.5 eV. (b) RPES data collected at several incident energies with four principal structures. The inset shows features that are the directly related to the charge disproportionate Fe sites.

RIXS spectrum was acquired for incident energies $h\nu_i$ across the Fe $L$ edge for three compounds in the series and shown in Fig. 3.6. There are several well-resolved structures that can be readily identified based on the energy loss of the excitations involved. At low energy losses, both the two insulating $LaFeO_3$ (Fig. 3.6(a)) and $x$ = 0.10 (Fig. 3.6(b)) doped samples exhibit three constant energy loss (also referred to as Raman-like) features at -5, -3.1 eV, and-1.8 eV (indicated by dashed lines) that signal intra-site Fe *d-d* excitations. These are typical of strongly correlated systems as observed in many other iron-based oxides[88–90]. The fixed energy loss features are assigned to

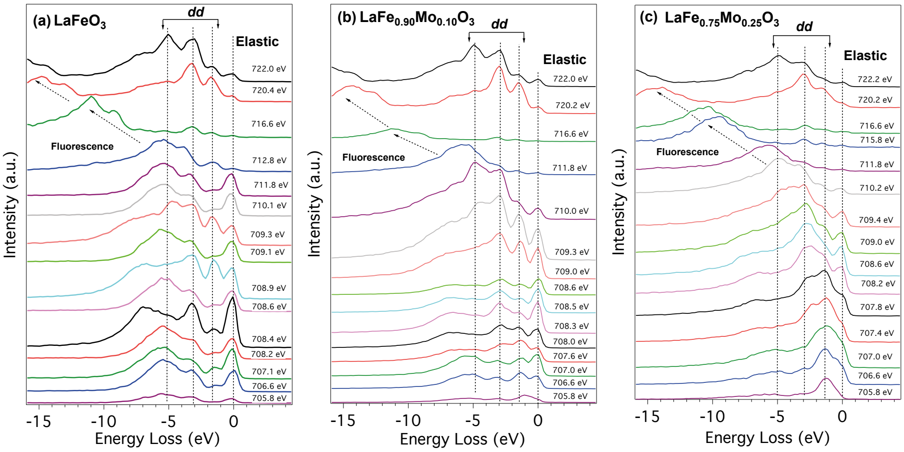

*Figure 3.6* Fe *L* edge RIXS spectra for (a) the undoped parent LaFeO$_3$, (b) $x = 0.10$ Mo doped sample, and (c) the metallic crossover at $x = 0.25$ at selected photon energies. The vertical dashed lines mark energy positions of inelastic loss features and arrows are used to guide the linearly dispersing fluorescence-like structure.

electronic excitations which involve localized states while excitations involving delocalized character linearly disperse with incident energy ($h\nu_i$)[71,72].

RIXS on LaFe$_{0.75}$Mo$_{0.25}$O$_3$ (Fig. 3.6(c)) clearly shows strong fluorescence contributions at low energy losses that are superimposed on top of the *d-d* excitations, which is a characteristic feature of metallic sample[91], where low energy excitations across the Fermi level are possible. As the fluorescence disperses to higher-energy with increasing incident energy, well-resolved features appear in its low-energy loss tail, with distinct *d-d* features at -3 eV, -1.6 eV, and -0.8 eV and remain at fixed energy loss with increase in incident energy. The peak positions shift to lower energy in metallic LaFe$_{0.75}$Mo$_{0.25}$O$_3$ compared to that of insulating LaFe$_{0.90}$Mo$_{0.10}$O$_3$ and LaFeO$_3$. The CT features are distributed across the different energy losses energies above -6 eV; this is in accordance with the modified Fe-O hybridization for the shorter Fe-O bond distance[81]. Furthermore, the RIXS spectra for the metallic sample exhibit clear low-energy loss intensities below 1 eV, providing a fingerprint to closing of the insulating gap. This signature has also been observed in many insulating-to-metallic transitions such as in NdNiO$_3$[91] and La$_{1-x}$Sr$_x$MnO$_3$[92].

The comprehensive x-ray spectroscopy results reveal an unusual metallic state with itinerant (Mo *d*) and localized carriers (Fe *d*) in LaFe$_{1-x}$Mo$_x$O$_3$.

## 3.3 The Double Perovskite $Sr_2FeMoO_6$

The results discussed in this section are obtained from x-ray spectroscopy measurements taken from Paper III. $Sr_2FeMoO_6$ (SFMO) has gained noteworthy attention due to its large changes in resistivity through application of small external fields – at room temperature[82]. Its electronic and magnetic properties are directly linked to the two TM cations and their interaction with each other and adjacent oxygen atoms[93]. Significant experimental and theoretical work has been done with the aim of describing the complex microscopic origin of its physical properties, however uncertainty still remains in regards to its ground state ionic configuration.

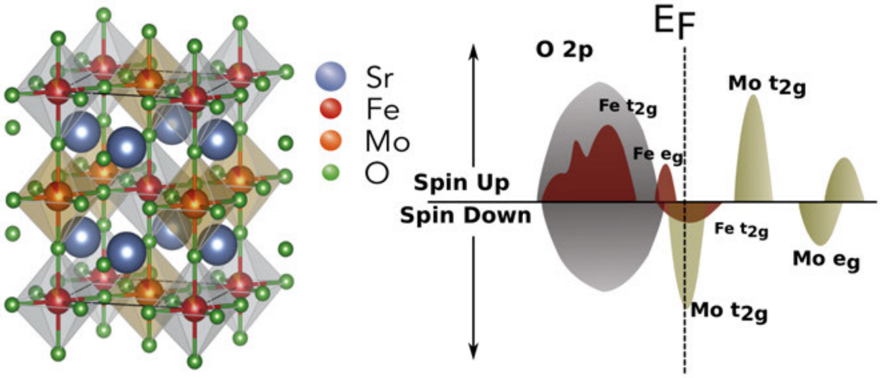

*Figure 3.7* Schematic of the tetragonal crystal structure for SFMO with alternating $FeO_6$ and $MoO_6$ octahedra in an ordered perovskite. (b) Schematic electronic structure that show metallicity from spin-polarized carriers in the spin-down channel.

In a completely ordered SFMO structure, the Mo and Fe alternate in a rock salt type order that repeats in all crystallographic axis as shown in Fig. 3.7(a). The magnetic ordering is usually considered as a ferrimagnetic state with parallel Fe moments that are antiferromagnetically aligned to Mo moments. This material is also noteworthy for its half-metallicity, meaning the density of the states for the down-spin band is present at the Fermi level, whereas the up-spin band forms a gap as shown in the schematic in Fig. 3.7(b).

In order to disentangle the Fe 3*d* and Mo 4*d* states in the valence band, resonant photoemission is aptly suited to separate the orbital-resolved *d* contributions. Figure 3.8(a) shows the RPES spectra taken across the Mo $L_3$ absorption edge measured in TEY mode. The $L_3$ structure is formed by a doublet structure at 2521.6 eV and 2525 eV (Fig. 3.8(a)), which agrees well with a previous study with multiplet calculations that assume a $Mo^{5+}$ ($4d^1$) valency[94]. In the RPES spectra shown in Fig. 3.8(b), one can easily distin-

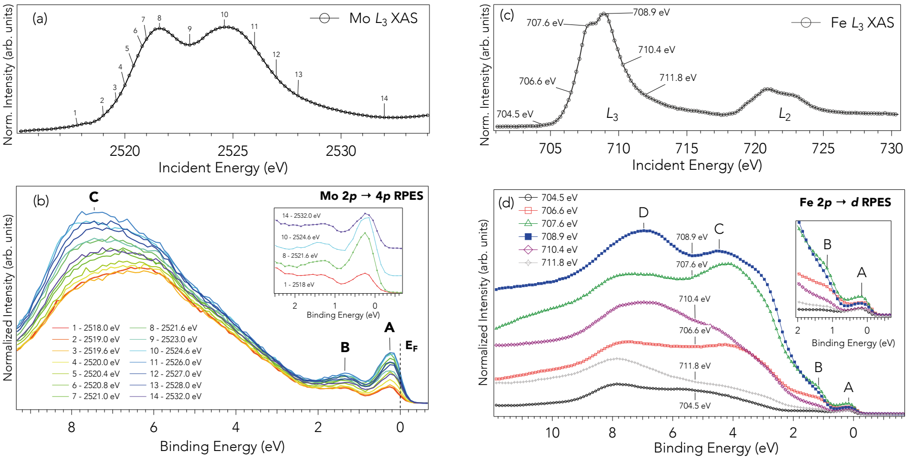

*Figure 3.8* (a) Mo $L_3$ XAS in TEY mode. (b) Mo RPES reveal three structures (marked 'A', 'B', and 'C') that related to Mo *d* states in the valence band. The *inset* shows a narrow VB range at off-resonance on resonance photon energies. (c) Fe $L_3$ XAS spectrum. (d) Fe RPES show four features (labeled A-D) that are enhanced at the absorption maximum (~ 708.9 eV) in contrast to incident energy below the absorption threshold (704.5 eV). The A and B features can be assigned to the $t_{2g}\downarrow$ and $e_g\uparrow$ respectively.

guish three well-defined structures labeled *A*, *B*, and *C* that are all modified by the incident energy across the Mo $L_3$ absorption edge. A finite density of states appears between 0.5 eV and the $E_F$ (feature labeled '*A*') at all photon energies, and enhanced at the maximum of the absorption threshold (labeled '8' in top panel of Fig. 3.8(a)). This prominent feature relates directly to itinerant Mo *d* states at the $E_F$, in agreement with previous results[95]. The broad *B* feature ranging from 0.8 – 2 eV can be assigned to an admixture of spin-up Fe $e_g\uparrow$ states and spin-down Mo $t_{2g}\downarrow$ states. The structure at 7-8 eV has also been argued to belong to Mo 4*d* states hybridized with O 2*p* bonding states[96]. These features together qualitatively show the energy positions and spectral density of the delocalized Mo *d* states in the valence band, a crucial component of the electronic description of SFMO.

The Fe *L* absorption edge and the resonant photoemission spectra are both shown in Fig. 3.8(c,d). The off-resonance case can be regarded with energy of 704.5 eV, below the Fe $L_3$ absorption threshold. The spectrum clearly shows a tangible number of states at the Fermi level due to Fe *d* states (Feature '*A*'), which can be assigned to the delocalized Fe $t_{2g}\downarrow$ spin states. The shoulder feature B, separated by about 1.25 eV from $E_F$, is attributed to the Fe $e_g\uparrow$ spin-up states. The energy separation between feature A and B can be associated with the spin-down $t_{2g}\downarrow$states and spin-up $e_g\uparrow$ states respectively. The significant enhancement of the states between 3 – 10 eV (labeled C and D in Fig. 3.8(d)) are due to strong Fe 3*d* – O *2p* hybridization. Feature C and

D at 5.5 eV and 4 eV respectively are ascribed to Fe $t_{2g}\uparrow$ and the Fe $e_g\uparrow$ bonding states that hybridize with the O 2 *p* states. These spectral signatures fall exactly in line with previous absorption and photoemission experiments[95], and are in line with proposed models that explain the metallicity in SFMO[82,93]. Accordingly, the RPES data shows that states with intensity at the Fermi level are due to both Fe 3*d* and Mo 4*d* states.

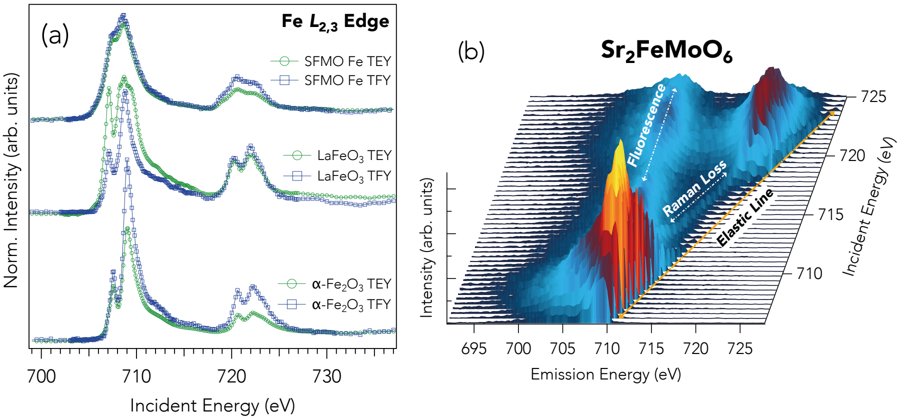

*Figure 3.9* (a) XAS measured in TEY and TFY for SFMO and two reference $Fe^{3+}$ compounds $LaFeO_3$ and α-$Fe_2O_3$. (b) A RIXS waterfall plot measured on an emission energy axis.

RIXS is another technique that can directly probe the valence electronic structure as well as the correlated nature of *d* orbitals. Fig 3.9(a) shows the near-edge XAS for SFMO and two related oxides with a $Fe^{3+}$ valence structure measured in both TEY and TFY. All three samples show a low-energy shoulder, which is common to compounds with a $Fe^{3+}$ formal valence [97,98]. The two groups of peaks near 710 eV ($L_3$) and 721 eV ($L_2$) are due to spin-orbit Fe 2*p* core levels, which are further split by the interplay of crystal-field splitting, charge transfer, and *p-d*/*d-d* interactions multiplet effects [99,100]. The RIXS spectrum is collected across the Fe *L* absorption edge is presented in a 3D waterfall plot in Fig. 3.9(b). The RIXS map is useful to visualize the low-energy excitations of the system as a function of different incident energies. The RIXS map in Fig. 3.9(b) show a constant emission energy fluorescence features centered at ≈ 709 eV and near ≈ 720 eV that are $L_\alpha$ and $L_\beta$ lines respectively.

To further analyze the RIXS spectra of SFMO, we compare the different energy loss features against the insulator α-$Fe_2O_3$ that also displays a weak magnetism at room temperature[101], as shown in Fig. 3.10. SFMO exhibits

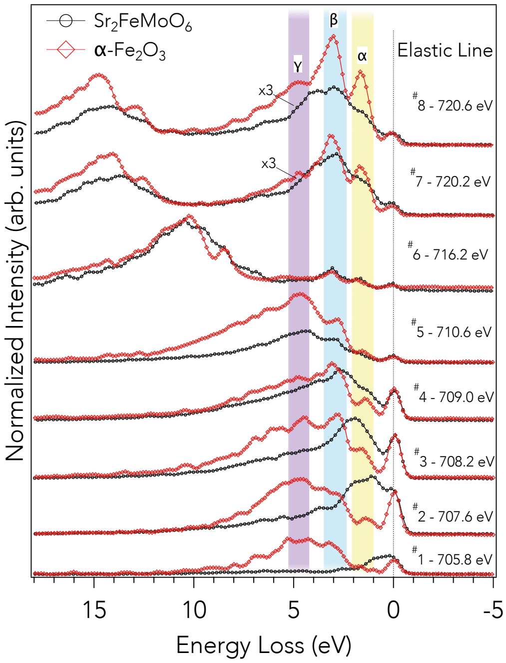

*Figure 3.10* RIXS 1D data presented alongside Fe$^{3+}$ α-Fe$_2$O$_3$. Energy loss features marked α, β, and γ correspond to *d-d* excitations.

very broad features clearly contrasting the well-resolved peaks for the insulating α-Fe$_2$O$_3$. The two Raman-like energy loss features centered at approximately 1.4 eV and 3.0 eV (marked α and β respectively in Fig. 3.10) for α-Fe$_2$O$_3$ can be assigned to intra-band *d-d* transitions between the Fe$^{3+}$ t$_{2g}$ and e$_g$ bands. The same features are also distinguishable for SFMO, although broader than that of α-Fe$_2$O$_3$. The inelastic features for SFMO are superimposed on top of fluorescence emission. A closer inspection reveals that the peaks that are well defined for α-Fe$_2$O$_3$ can also be tracked at constant energy loss with increasing incident energies for SFMO, particularly at excitation energy of 716.2 eV. These features are typical for crystal field excitation in correlated materials with *3d* transition metal elements[71,72]. The early onset of the fluorescence-like structure on the SFMO sample can be attributed to the half-metallic nature of the sample. The larger bandwidth of the inelastic structures for SFMO in the low energy excitation range, from 3 - 6 eV, must also include inter-band transition from Mo *d* manifold to Fe t$_{2g}$ and e$_g$ states. This can be sensibly argued due to the extensive hybridization of Mo *d* states that appear alongside Fe *d* states as highlighted through RPES data. Despite these assessments, further studies of the Mo *L* RIXS, corroborated by *ab initio* calculations can provide key information on the coupling between Fe and Mo ions.

# 4 Bulk and Thin Films of a Doped BaTiO$_3$

In this chapter, a comprehensive x-ray spectroscopy results are presented on a co-doped ferroelectric BaTiO$_3$ (BTO). Much of the work presented in this section is taken from the conclusions in Paper IV and V.

## 4.1 Low Bandgap and Ferroelectricity of co-doped BaTiO$_3$

This chapter presents the work on bulk and thin film ferroelectrics based on BaTiO$_3$. BaTiO$_3$ (BTO) is one of the most well studied ferroelectrics and used in many different applications[102–106]. However, the large bandgap of BTO ($E_g$: 3.2 eV) can harvest only a tenth of the solar irradiation, making it unsuitable for the light absorption in the visible spectrum.

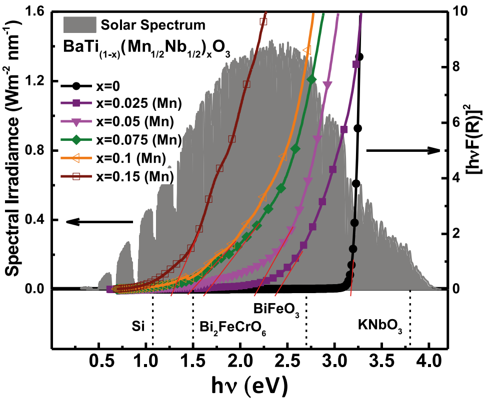

*Figure 4.1* Change in optical band gap with increase in concentration of dopants. Band gaps of a few standard photovoltaic materials are also indicated. Figure adapted from Ref. [107].

In this context, our research team used a double-element doping strategy to reduce the bandgap of BTO to the visible region of the spectrum without compromising the polarization. The co-doping at the Ti-site of BaTiO$_3$ with trivalent Mn$^{3+}$ and a $d^0$ Nb$^{5+}$ ions (BaTi$_{1-x}$(Mn$_{1/2}$Nb$_{1/2}$)$_x$O$_3$) showed an appreciable reduction in the bandgap and a sizable retention of the remnant polarization[107]. The partially occupied Mn $3d^4$ should meet the prerequisite for bandgap variation[30,108] and the charge-compensator $Nb^{5+}$ may provide an off-centering similar to that in $KNbO_3$[109]. In Fig. 4.1, bandgap values for different compositions for $BaTi_{1-x}(Mn_{1/2}Nb_{1/2})_xO_3$ series (hereafter referred as BTMNO) is obtained through UV-Vis diffuse reflectance spectra. The bandgap continuously decreases from 3.18 eV for pure BTO to 1.3 eV for the composition with $x = 0.15$. The polarization was found to be largely preserved, with a sizable room-temperature polarization of 15.4 μC/cm$^2$ for the $x = 0.075$ sample, 70% of the parent $BaTiO_3$ (25 μC/cm$^2$).

Here, we probe the changes in the electronic structure as a function of doping using combined x-ray spectroscopies. First, we monitor the displacement of Ti atom using the pre-edge structure at the Ti *K* edge as shown in Fig. 4.2(a). The first two peaks in the magnified pre-edge spectra ($A_1$ and $A_2$ in Fig 4.2(b)) directly relate to the quadrupolar $1s \rightarrow 3d$ $t_{2g}$ and mixed Ti $e_g$ - O $2p$ transitions respectively[110,111,66]. The intensity of peaks $A_2$-$A_5$ decrease progressively upon increased doping with Mn/Nb ions when compared to $BaTiO_3$. The extent of off-centering of Ti atom can be directly related to the relative change in intensity of the pre-edge $A_2$ peak[112,113]. The area under peak $A_2$ is estimated with a combination of Gaussian and an arctangent background, exhibits the same trend as the $P_R$ as a function of doping as shown in Fig. 4.2(c). The increase in $P_R$ for the $x = 0.075$ sample compared to $x = 0.05$ is also reflected by a corresponding increase in the $A_2$ peak area from the Ti *K* pre-edge spectra. This finding indicates that the Ti atom is still off-centered with respect to the octahedral cage of surrounding oxygen atoms, thereby retaining ferroelectricity in presence of doping of $3d$ (Mn) and $4d$ (Nb) transition metals.

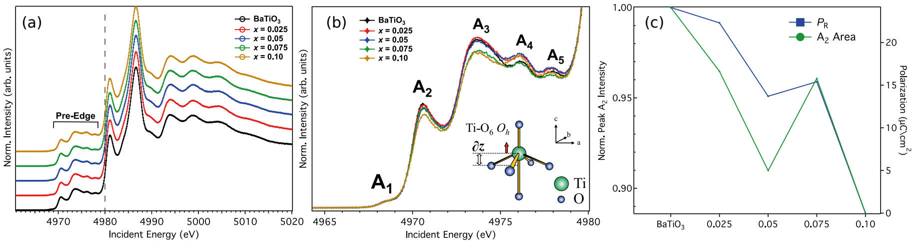

*Figure 4.2* (a) Ti *K* edge HERFD-XAS for all compounds. (b) Pre-edge feature that show a minor change in the intensity of the quadrupolar transitions (peaks $A_1$ and $A_2$) and indicate that the Ti off-centering is maintained. (c) The polarization behavior is consistent with measured $A_2$ peak intensity for the bulk samples.

To understand the changes in the valence electronic structure as result of dopants, we use resonant photoemission at the Mn *L* edge. The resonant process at the Mn core $2p$ states enhances the Mn $3d$ spectral weight, making it feasible to characterize the Mn $3d$ states and their position in the valence band. Figure 4.3(a) shows the RPES on thin films collected at the maximum of Mn $L_{2,3}$ absorption edge. As shown by the resonant enhancement, electronic states near $E_F$ has Mn $3d$ character. The on-off resonance difference spectra, denoted by the gray shaded area (Fig. 4.3(a)), provides a direct probe for Mn $3d$ states. Although the spectral shapes are similar, the intensities of all three peaks, $C_1$, $C_2$, and $C_3$ (Fig. 4.3(b)) show a larger enhancement for $x = 0.075$ when compared with $x = 0.025$ film, i.e. increasing intensity with an increasing Mn content, as expected for these newly created Mn states. From the RPES data presented here, we find the dopants shift the valence band edge by as much as 1 eV relative to the Fermi level ($E_F$). Thus, the growth of new states with predominantly Mn $3d$ character within the bandgap of BTO (marked $C_1$ in Fig 4.3(b)) can be linked with the observed bandgap reduction. This finding corroborates with DFT+U calculations that clearly show formation of new states at the top of the valence band edge with predominant Mn $3d$ character (*see* Fig. 4.3(b)).

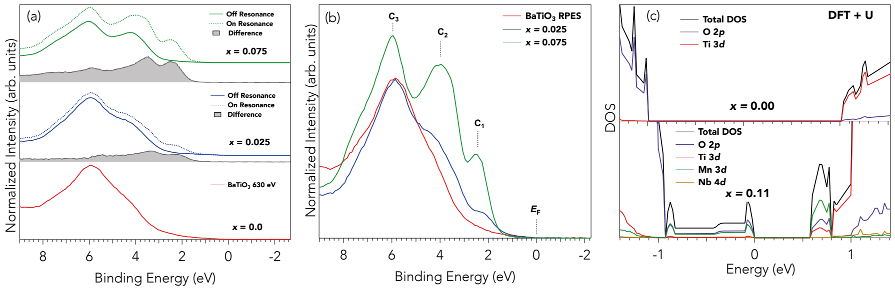

*Figure 4.3* (a) RPES spectra for doped and undoped samples at the Mn *L* edge in the off-resonance ($h\nu_i = 630$ eV) and on-resonance condition ($h\nu_i = 640.2$ eV). (b) The three resonating features for $x = 0.025$ and $x = 0.075$ are assigned to Mn *d* states. (c) Total and partial orbital-projected density of states for $BaTiO_3$ (top) and $x = 0.11$(bottom).

## 4.2 Thin Film Properties of co-doped $BaTiO_3$

In order to realize the unique properties of BTMNO for use in ferroelectric photovoltaics, high-quality thin films are fabricated by pulsed laser deposition (PLD). We explore Mn/Nb doping levels for $x = 0.025$, which in our previous study of bulk materials, was found to exhibit the highest saturation

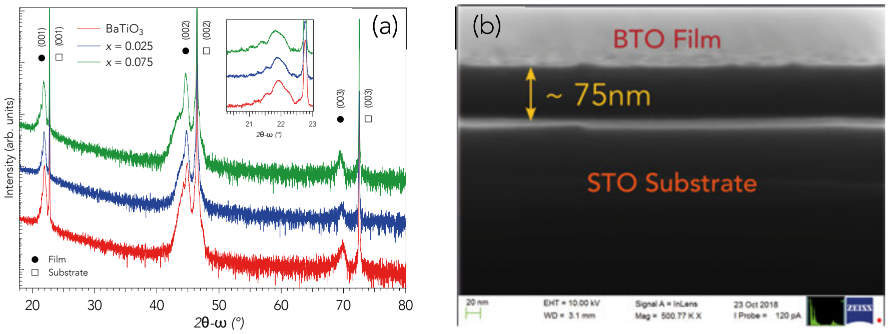

*Figure 4.4* (a) XRD scans of BTO and $Mn_{1/2}Nb_{1/2}$ doped BTO thin films. (b) cross-sectional SEM image showing the thickness and a uniform BTO film on $SrTiO_3$.

polarization of 22.3 μC/cm$^2$, and $x = 0.075$ (lowest band gap) in addition to the parent $BaTiO_3$ thin films. The thin films were fabricated on (001) $SrTiO_3$ substrates with a 0.1° miscut to assure a layer-by-layer growth. The high-resolution diffraction pattern is shown in Fig. 4.4(a). The three clear diffraction peaks correspond to (00*l*) reflections signifying epitaxial growth and no indication of any secondary phases is observed. The position of the (002) peaks systematically shifts toward lower angles with increasing Mn/Nb content, suggesting the two transition metals occupy the B-site. The out-of-plane lattice parameters calculated from the (002) reflections are 4.366 Å, 4.376 Å, and 4.386 Å for BTO, BTMNO-25, and BTMNO-75 respectively. The *a*-axis lattice parameter for bulk BTO is 3.992 Å[114], indicating that all three films are strained due to the mismatch with the STO substrate (*a*-axis 3.905 Å). The inset of Fig. 4.4(a) shows expanded region around the (001) peak, with reflections clearly displaying interference fringes suggesting a relatively coherent and a smooth interface with the $SrTiO_3$(001) substrate. From the cross-sectional SEM images in Fig. 4.4(b), it can be observed that the thickness of the BTO layer is ~ 75 nm.

AFM images taken across the film surface are shown in Fig. 4.5(a)(b). Since the samples are grown on an STO substrate with a 0.1° miscut, the step-terrace structure of the deposited film following post-annealing is clearly observed in the AFM image shown in Fig. 4.5(a). This clearly indicates atomically flat terraces with single unit-cell steps (~ 4 Å). For thicker films, 3D clusters nucleate on these layers due to the stress induced by the lattice mismatch (Fig 4.5(b))[115].

The bandgap of the films are characterized using a UV-Vis spectrometer in the total reflectance mode as shown in Fig. 4.5(c). The bandgap of $BaTiO_3$ has previously been reported to be nearly 3.18 eV, just outside of the visible spectrum[107]. Here, the optical band gaps can be estimated from the tangent

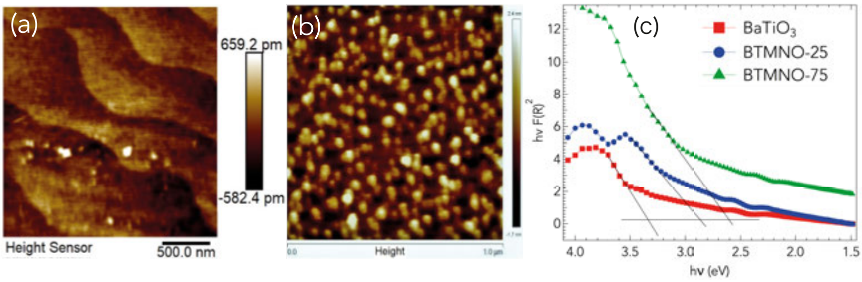

*Figure 4.5* AFM images of (a) 75 nm doped BTMNO-75 film with well-defined terraces indicating layer-by-layer growth. (b) 125 nm $BaTiO_3$ thin films with 3D nucleated clusters. (c) UV-Vis measurements in reflectance mode for BTO, BTMNO-25, and BTMNO-75 thin films with a bandgap tuning from 3.2 eV to 2.6 eV.

lines in the $(\alpha h\nu)^2$ versus $h\nu$ plots for the three samples. The BTMNO-75 shows a bandgap of approximately 2.6 eV, enabling the absorption of sunlight in the visible range, lower than that for BTO (3.2 eV) thin film. This is in line with our report on polycrystalline samples, where the bandgap reduction was shown to result from Mn *d* states that hybridize with O 2*p* states at the edge of the valence and conduction bands[116].

The ferroelectric hysteresis loops can be revealed through the PFM response. This technique has developed into a successful tool for direct evidence of ferroelcitrcity[77,117,118]. Figure 4.6(a)-(c) show a hysteretic behavior typical of polarization switching for all three samples. The top panel shows the amplitude switching and bottom panel shows the phase switching as function of bias. The PFM phase-voltage curve shows a fully saturated hysteresis for the

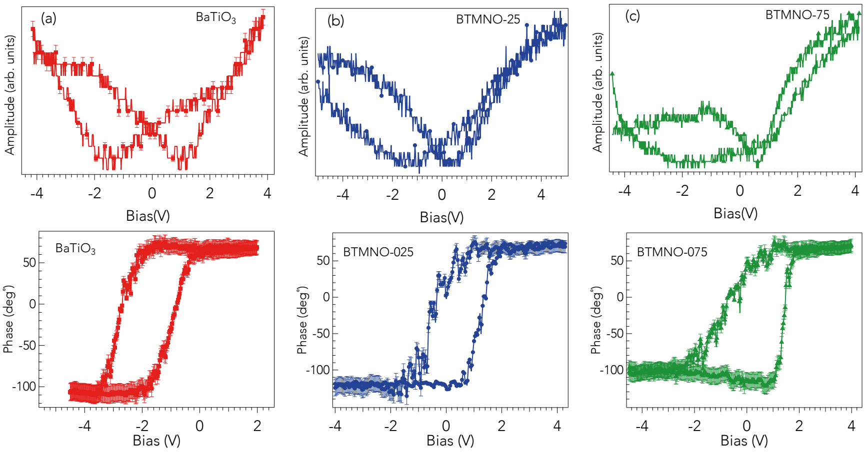

*Figure 4.6* PFM local amplitude (top panel) and hysteresis phase loops (bottom panel) for 75 nm films of (a) $BaTiO_3$, (b) BTMNO-25, and (c) BTMNO-75.

BTO and doped BTMNO samples. All curves show an 180° phase change across the saturation voltages, signifying complete switching, which is characteristic to a true ferroelectric. The hysteresis for BTMNO-075 shows a slight anti-symmetric phase with respect to negative DC bias, which can likely be attributed to defect-induced polarization pinning in the upward direction[119–122]. We note here that the hysteresis loop is offset towards a negative voltage indicating a built-in electric field that is also found in similar studies[119]. The amplitude curves (Fig. 4.6 *top panel*) show a nearly symmetrical butterfly shape for the $BaTiO_3$ sample, which indicates a robust and switchable ferroelectricity. The curve is slightly anti-symmetric for BTMNO-25 and BTMNO-75 thin film samples likely due the strong poling for doped thin films. Both hysteresis and butterfly loops however are characteristic of classical ferroelectric switching.

To demonstrate the effect of poling on ferroelectric switching of the thin film, we reverse the upward polarization by scanning a diagonal line across the film surface with a tip biased with a voltage $V_{\mathrm{Tip}} = +5$ V that exceeds the coercive voltage for the film. Figure 4.7 shows the resulting polarization pattern as measured by PFM for the BTMNO-25 sample. The antiparallel domain line shows a clear contrast with the polarization in the opposite direction, showing the polarization response is strong with domain switching. A negative bias of $V_{\mathrm{Tip}} = -5$ V was written in a mirror opposite line and reversed polarity (*not shown).* Overall, the PFM images show clear hysteresis behavior for all three films and the ability to switch polarization with a biased tip.

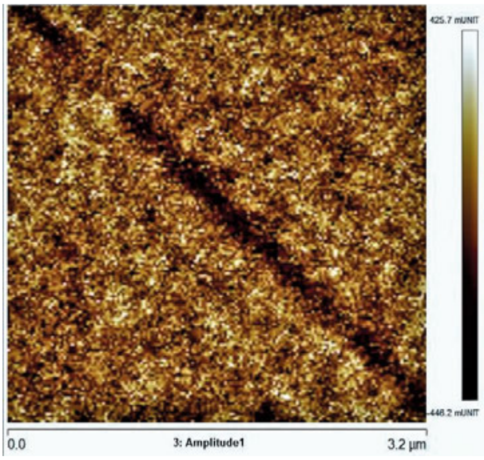

*Figure 4.7* Vertical PFM image for BTMNO-25 after applying a $V_{\mathrm{Tip}}$ +5 V over a 3 x 3 $\mu m^2$ area.

# 5 Halide Perovskites

In this chapter, the results of the perovskite halide compounds are highlighted. The following chapter is based on results in Papers VI-X. The first portion of this chapter focuses on perovskite halides with Pb as the post-transition metal cation and their low-dimensional equivalents. The subsequent section addresses the lead-alternative based halides and their electronic structure. And lastly, we report on nanocrystal halide perovskites used in a high-efficiency photovoltaic device.

## 5.1 Low-Dimensional Halides

Low-dimensional perovskite halides have emerged in the past few years largely catalyzed by the interest in stable halide solar cell materials. Their impressive efficiencies and remarkable stability relative to their 3D counterparts ($CH_3NH_3PbI_3$) has put this subclass of materials into broader focus and hold promise in energy-related applications[123–125]. The primary interest is on the x-ray spectroscopy, and how the reduced dimensionality effects the electronic and band structures and it includes attempts to relate the spectroscopic findings to the material properties.

In Paper VI, we report on the role of synthetic routes that form two completely different structures. The one-dimensional (1D) structure, $(BdA)Pb_2I_6$ (BdA: butyl-1,4-diammonium), forms a one-dimensional inorganic chain with a disordered intercalation of the organic bications. The large cation causes the connectivity of the inorganic units to be lost in one or more dimension in the perovskite network. The byproduct of a different synthetic route produce a two-dimensional structure in which $(BdA)PbI_4$ (001) structural planes to consist of octahedral corner sharing lead-iodide planes and organic bications separating the inorganic layers. The varying bond distances and angles are known to influence the orbitals that contribute to bonding of these materials[126], and therefore the electronic structure can bear information to these structural changes.

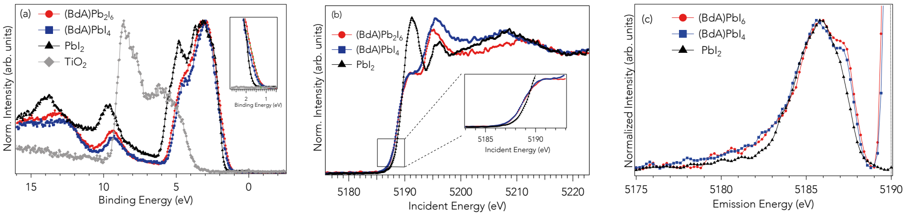

*Figure 5.1* (a) Valence levels of the TiO$_2$ film, PbI$_2$ and (BdA)Pb2I$_6$ and (BdA)PbI$_4$ measured with a photon energy of 4000 eV. (b) Plots of the unoccupied *np* states of iodine in the conduction band and (c) RIXS spectra for (BdA)Pb2I$_6$, (BdA)PbI$_4$, and PbI$_2$.

Figure 5.1(a) shows the HAXPES spectra and x-ray absorption and emission spectroscopy on the two compounds deposited on a mesoporous TiO$_2$ thin film substrate. The inset in Fig. 5.1(a) shows slight differences in the valence band edge position for the 1D and 2D material compared to the precursor PbI$_2$, with a small shift for the 2D-(BdA)Pb$_2$I$_6$ towards smaller binding energies. It was shown in Paper VI that the Pb 4*f* core-level shifts between the layered compounds are small (0.05 eV), however for I 3*d*, the core-level shift for (BdA)Pb$_2$I$_6$ and (BdA)PbI$_4$ is about 0.12 eV. This data gives evidence that the positions of the valence band position shift largey due to iodine *p* orbitals.

In order to map the I *p* projected density of states, results from element-specific HERFD-XAS and RIXS at the I $L_2$ edge is shown in Fig. 5.1(b,c). The absorption spectrum at the I $L_1$ edge is a reflection of the unoccupied *p* density of states and coordination. The two data sets clearly show a similar spectral profile, but vary in intensity and energy position for the different structures, a change in the local structure. RIXS spectra in Fig 5.1(c) show a shoulder feature on the higher energy side of the spectrum that can be linked to changes in the hybridization with Pb 6*s* states. The Pb-I-Pb bond length for the 1D compound is 6.08 Å as compared to 6.16 Å for the 2D compound. These small changes to the local structure can affect the orbital overlaps of Pb and I states, and thus reflect in small changes to the electronic structure.

In low-dimensional perovskites, the organic cation ionic radii and length is associated with varying structural properties that result in the tunability of material properties such as bandgap and excitons binding energies[124,127–130]. The next study is extended to tuning the inter-layer separation distance between the single PbI$_6$ octahedral layer ($n = 1$), as highlighted in Paper VII. The organic cation length is varied between the ~4 Å (BdA, butyl-1,4-diammonium), 6Å (HdA, hexyl-1,6-diammonium), and 8 Å (OdA, octyl-1,8-diammonium) and the changes to the electronic structure is surveyed through different x-ray spectroscopies. In contrast to the layered PbI$_2$, the observed structural changes in the 2D hybrid materials results in a dimensional constraint of the inorganic layer. The narrowing of VB states is demonstrated by a closer inspection of the valence band profile as shown in Fig. 5.2(a). This is an indication that the organic cation-linked 2D perovskites constitute more localized bands than $PbI_2$ and $MAPbI_3$. The valence bandwidth narrows as we go from the layer-separated $PbI_2$ to the 3D $MAPbI_3$, and lastly to the interlayer-separated compounds.

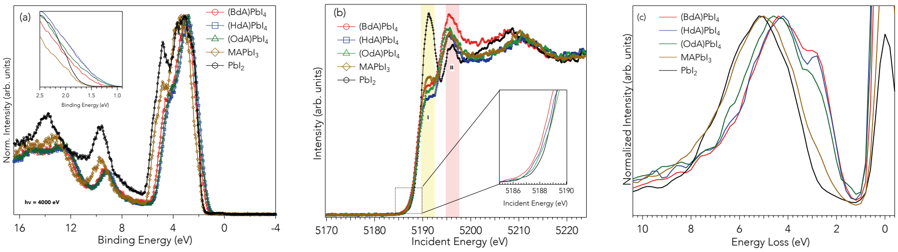

*Figure 5.2* (a) The VB photoemission spectra collected for all compounds at 4000 eV. (b) HERFD-XAS at the I $L_1$ edge that is projection of unoccupied I *p* states, and (c) RIXS spectrum plotted on an energy-loss scale.

To evaluate iodine's role in modifying the frontier valence states, we exploit the element-specific nature of HERFD-XANES and RIXS at the I $L_1$ edge to probe occupied and unoccupied states as shown in Fig. 5.2. The structural changes are evident from the lineshape of the I $L_1$ absorption spectra shown in Fig 5.2(b). An increase in intensity implies a larger number of unoccupied states for $(BdA)PbI_4$ at regions marked I and II in the spectra. This increase may be the consequence of lower symmetry compared to $(HdA)PbI_4$ and $(OdA)PbI_4$, which is seen by minor changes to lattice positions as well as octahedral tilt. The change in interlayer distance also modifies the bandgap of the materials, with 2.37 eV for the BdA compound and 2.55 eV for the HdA perovskite. This effect can be seen in shifting of I 5*p* states toward lower energy loss for $(BdA)PbI_4$ followed by $(HdA)PbI_4$ and $(OdA)PbI_4$. This trend follows the sequence of increasing band gap from (BdA)PbI4 (2.37 eV), (HdA)PbI4 (2.44 eV), and (OdA)PbI4 (2.55 eV) and is in agreement with the photoemission spectra reported earlier.

In order to support the experimental evidence for band narrowing as result reduced dimensionality, DFT calculations based on Generalize Gradient Approximation (GGA) is presented in Fig. 5.3. The calculations highlights the contribution of Pb 6*s* and I 5*p* states in the VB and CB edges. As is clearly seen in Fig 5.3(a), the band narrows as the materials adopts a reduced dimensional structure as compared with $PbI_2$ or $MAPbI_3$. This is particularly evident for I states. The interactions between the interlayers show a directional dependence, where I *p* states are mostly affected in the axial direction as shown in Fig 5.3(b). This demonstrates the orbital confinement effects in lower dimensional perovskite halides.

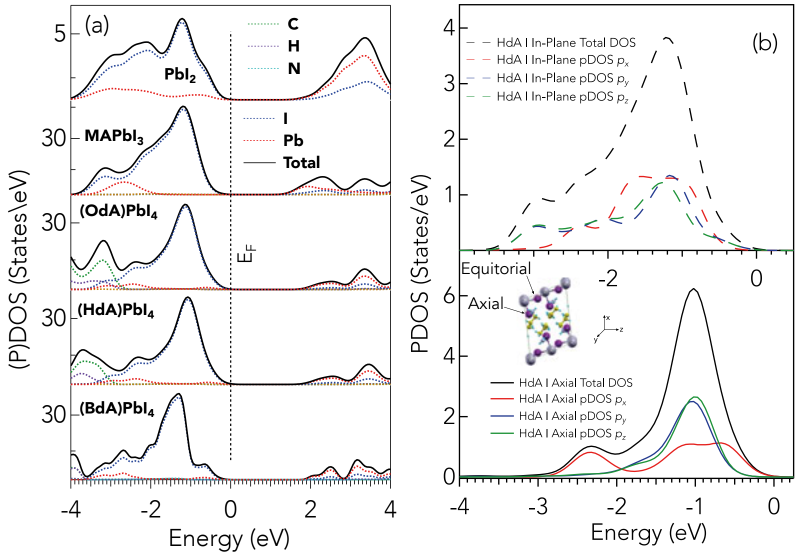

*Figure 5.3* (a) Calculated total and partial density of states (DOS) of 2D perovskites plotted alongside $PbI_2$ and 3D $MAPbI_3$. (b) Partial and total DOS for iodine in $(HdA)PbI_4$ showing the contribution to from both axial and equatorial iodine atoms. The effect of dimensionality clearly has an effect on the orbital narrowing for iodine in the axial direction.

The band structures also show a directional dependence on the effect mass of charge carriers for all three layered compounds. A small carrier mass is observed for the in-plane direction within the inorganic planes and much larger perpendicular to the inorganic plane, shown in Fig. 5.4. This is in line with the expectation that the charge transport mainly occurs within the inorganic network[131,132]. In addition, a band dispersion for the direction perpendicular to the inorganic network is observed for the shortest alkyl chain $(BdA)PbI_4$ perovskite (Figure 5.4(a)), showing an interaction and possible charge transport between the layers. This dispersion becomes flatter for $(HdA)PbI_4$ (Fig. 5.4(b)) and disappears for the $(OdA)PbI_4$ (Fig. 5.4(c)). This reveals that for distance longer than 6Å limit, there is no interaction between inorganic interlayers.

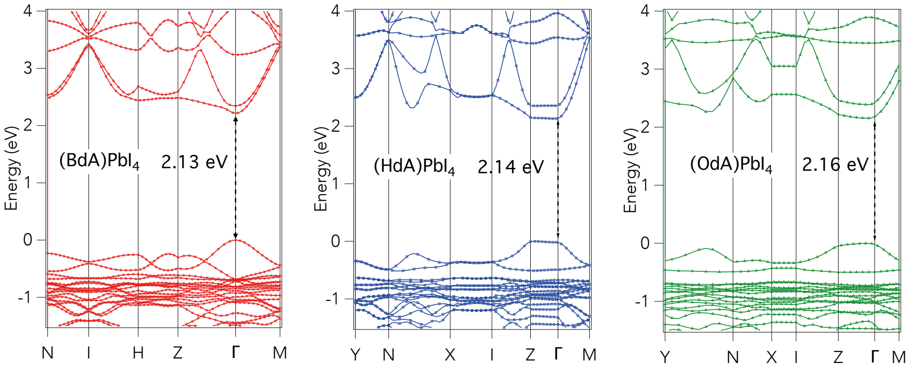

*Figure 5.4* Band structure plots for (a) (BdA)$PbI_4$, (b) (HdA)$PbI_4$, and (c) (OdA)$PbI_4$ together with K-space paths with the first Brillouin zone and their estimated band gap values calculated with DFT.

## 5.2 Lead-Alternative Halide Perovskites

There is an ongoing effort to find new materials that can substitute lead with properties similar to that of lead-based compounds. The commonly used lead-based perovskite are associated with toxicity and concerns about ambient stability[15–17], and necessitating the pursuit of alternatives beyond the lead-based structures. The choice of a divalent cation not only determines the crystal unit structure, but also tunes the optical properties of the resultant material. Several studies suggest the $Pb^{2+}$ cation plays a definitive role in determining the electronic structure of Pb-based perovskites, particularly at the valance and conduction band edges[23,133]. Metal substitutions by $Sn^{2+}$, $Sb^{3+}$, and $Bi^{3+}$ are most suitable due their similar ionic radii and valence electron configuration, $ns^2$. The incorporation of these materials in solar cell devices is still at its nascent stage, however have demonstrated good results that merit further investigation[134].

The electronic structure of the Pb-based perovskites maintains a stable $Pb^{2+}$ oxidation state that results in a mostly 3D crystal structure. The different valency and ionic radii imposed by a substituted cation imposes steric hindrance that can trigger the formation of a lower symmetry structure or layered systems. Regardless, it is likely that the principal building block in the crystal structure is a $MX_6$ octahedra that can be joined in corner-sharing, edge-sharing, or vertex-sharing and repeated along a crystallographic direction. It is well established that the A-site cation determines the structure, stability, and bandgap of the material. However, it is preferentially ionic and has shown to have minor influence on the band edge electronic structure.

Therefore, the electronic structure information obtained through various experimental and theoretical methodologies can serve as an appropriate comparison against the best performing HP material.

In Paper VIII, x-ray spectroscopy results on bismuth-based halide materials ($Cs_3Bi_2I_9$ and $BiI_3$) are discussed. Bismuth-based hybrid perovskites also bear similarities to the Pb-based analogues that also adopt a stable $d^{10}s^2p^0$ electronic configuration with covalent Bi 6*p*/6*s* and I 5*p* at the top of the valence band and mostly Bi 6*p* at the bottom of the conduction band[135]. It was suggested that this specific orbital occupancy leads to anti-bonding states that form defect states that largely lie within the valence band, a desired attribute to reduce carrier recombination[53,135,136]. The experimental x-ray results are compared against DFT calculations.

We first probe the *bulk* valence band structure for the two bismuth compounds and the related precursor CsI using HAXPES as shown in Fig. 5.5. The overall lineshape of $Cs_3Bi_2I_9$ has similarities to the precursor, with modification in the valence band edge position in between the low bandgap $BiI_3$ and high bandgap CsI ($BiI_3$: 1.67 eV, $Cs_3Bi_2I_9$: 2.2 eV, CsI: 6.3 eV). The doublet peak near ~ 12 eV corresponds to Cs 5*p* orbitals, states that do not participate in bonding as expected. The calculated partial and total density of states (DOS) for both $Cs_3Bi_2I_9$ and $BiI_3$ alongside the HAXPES data is presented in Fig. 5.5 (b). The DFT results are in close agreement to the experimental data. The I *p* states have substantial weight at lower binding energies of the valence band, and hybridize with Bi 6*s* lone pair states towards the edge of the valence band.

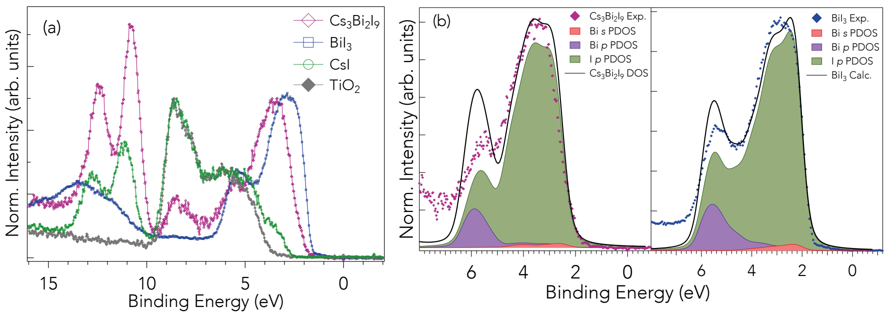

*Figure 5.5* (a) Valence band spectra for the three samples at 4000 eV (b) calculated and experimental VB for $Cs_3Bi_2I_9$ and $BiI_3$ along with experimental spectra.

HERFD-XANES and RIXS taken at the I $L_1$ edge are shown in Fig 5.6 along with the projected DOS using the Local Density Approximation (LDA) with Spin-Orbit Coupling (SOC). All three samples show distinct spectral characteristics due to the different coordination and displacement of iodine atoms in the unit cell. The absorption edge, defined at the maximum of the second derivative of the absorption spectrum, shifts to higher energy for $Cs_3Bi_2I_9$ and CsI and correlates with the concomitant increase in bandgap (see Fig. 5.6(a)). The RIXS presented in Fig. 5.6(b) on an energy loss scale is characteristic of occupied I 5*p* states. The energy difference between the elastic peak and the onset of the inelastic structures on the energy loss scale correlates with the size of the band gap in these compounds. Therefore, the shift of such an onset to a lower energy loss by 0.4 eV in $BiI_3$ as compared with $Cs_3Bi_2I_9$ indicates a small band gap in the former. This information can provide insight into the changes of I *p* states, and how they ultimately affect the band gap.

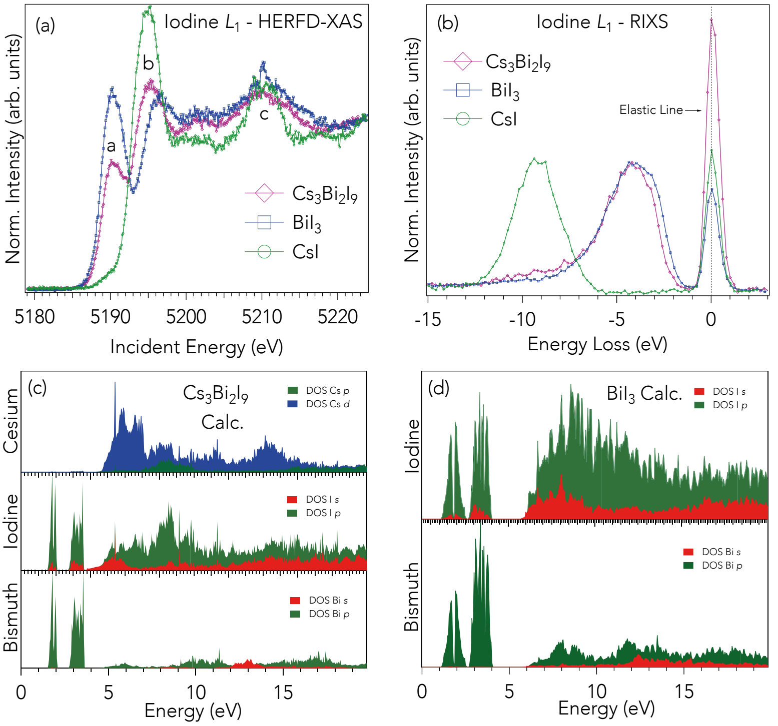

*Figure 5.6* (a) HERFD-XAS taken at the I $L_1$ edge for all three samples. (b) RIXS spectrum plotted on an energy loss scale. The projected unoccupied density of states for (c) $Cs_3Bi_2I_9$ and (d) $BiI_3$.

We now extend the study of bismuth compounds with the commonly used cation methylammonium (MA) at the A-site of the $A_3M_2X_9$ structure as outlined in Paper IX. The large cation and the mismatch in ionic radii force the structure to adopt a HP-like structure that results in a $(CH_3NH_3)Bi_2I_9$ compound, in a iododi-bismuthate crystal structure ($A_3Bi_2I_9$). This material has exhibited promising optoelectronic properties, with a photovoltaic efficiency of nearly 4% based on a optimized thin-film deposition technique[137]. The vapor assisted solution process (VASP) at different reaction times yielded tunable optoelectronic parameters, a highly uniform and compact film, improved stoichiometry, reduced metallic content, and desirable absorbing properties[138].

HAXPES was used to investigate the bulk electronic levels of $MA_3Bi_2I_9$ (MA: $CH_3NH_3$) synthesized at various reaction times in the VASP process. The two precursors, MAI and $BiI_3$ as subjected to varying annealing times after spin coating. The transition from the two precursors to the desired material can be monitored using the core-level photoelectron signals. An approximate estimation of the material stoichiometries can be made using the relative intensities of the experimental core levels and taken differential photoionization cross-sections into account[139]. The stoichiometry estimation for I/Bi is listed in Table 1, with values reasonably close to the expected value of 4.5. This stoichiometry points to marginal iodine deficiencies within the crystal, a common bulk defect found in many organometallic halides[140].

*Table 5.1* HAXPES stoichiometry data for the measured samples.

| **Sample** | **$BiI_3$** | **$BiI_3$ + MAI 5 min** | **$BiI_3$ + MAI 15 min** | **$BiI_3$ + MAI 25 min** | **$BiI_3$ + MAI 45 min** |
|---|---|---|---|---|---|
| I 4*d*/Bi5*d* | 3.03 | 4.31 | 4.30 | 4.50 | 4.28 |
| I 3*d*/N1*s* | - | 2.94 | 2.95 | 2.82 | 2.46 |

The experimental Bi 4*f* and valence band signals are presented in Fig. 5.7(a). The main contribution of the Bi 4*f* single is around 159 eV, indicating a $Bi^{3+}$ oxidation state[141]. The shoulder peaks at lower binding energy (~157 eV) is metallic $Bi^0$, which is likely due to the decomposition organic metal halides and $BiI_3$.[142] As the reaction time is increased, the detrimental metallic $Bi^0$ content is reduced, concurrent with photovoltaic efficiencies and improved film quality, demonstrating the effectiveness of longer vapor exposure times. Although the MA cation is much larger than the Cs atom studied previously, the optical transition is expected to be the same[143], as shown in the valence band profile in Fig. 5.7(b). The dashed red line (*see inset* Fig. 5.7(b)) indicates where the linearly extrapolated experimental spectra intersect with the baseline, an estimated measure of the valence band edge position. The VB offset are approximately the same for the entire set, except for reaction time of 5 min, which has a substantially higher metallic bismuth concentration. The energy position of the valence band maximum lie mostly in line with

$BiI_3$, indicating the corner-sharing counter cation $CH_3NH_3^+$ seems not relevant to the density of states in the valence band edge. The features between 3-5 eV is composed of I 5*p* and Bi 6*p* and lone pair $6s^2$ anti-bonding states, similar to that of the $Cs_3Bi_3I_9$ compound discussed in the previous section.

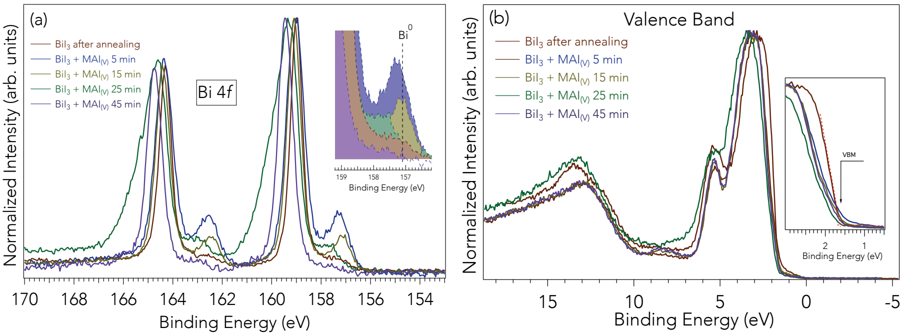

*Figure 5.7* (a) Core-level peak for Bi 4*f* showing a decrease in metallic content with deposition times. (b) Valence band spectrum for all samples and the annealed $BiI_3$ film and $BiI_3$ + $MAI_{(v)}$ for different reaction time.

In the previous sections, lead-alternative halides with Bi at the post-transition metal cations compounds were investigated in terms of their electronic structure. There are several other compounds that are related to this topic, however the results are not compiled into a manuscript. Regardless, it is worth highlighting some of these preliminary results. A recent HAXPES study was conducted on three post-transition metal HPs all with a lone pair valence configuration ($Sb^{3+}$: $5s^2$, $Pb^{2+}$: $6s^2$, and $Bi^{3+}$: $6s^2$). The cation at the A-site was varied between the smaller inorganic Cs and the larger and organic methylammonium (MA). The valence band photoemission spectrums are shown in Fig. 5.8 and are normalized to peak maximum near 3.5 eV for all samples. The larger cation $MA^+$ pushes the valence band edge closer to the Fermi level for all three post-transition metal compounds, suggesting the materials may become more n-type. The reported bandgap values from previous studies have shown to be smaller for MA to that of Cs-based halides[141]. This suggests that the cation size plays a definite role in alternating the bandgap as well the position of the valence band maximum (VBM). The $Sb^{3+}$ HPs show a pronounced structure near 1.3 eV, which has been showed to belong to lone-pair 5$s^2$ states based on band structure calculations[144,145]. The peculiarities of the electronic structure and the projected density of states near the band edges need further investigation through complimentary spectroscopy techniques, the intentions of future work.

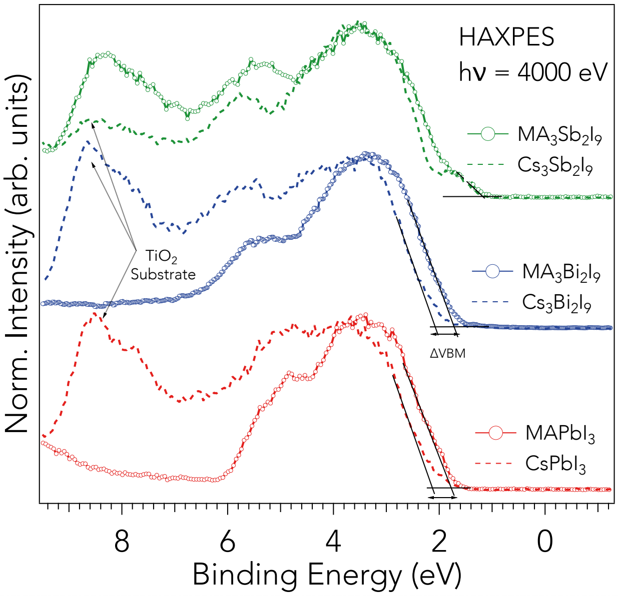

*Figure 5.8* HAXPES VB spectra for HPs with three different B-site metal: $Sb^{3+}$, $Bi^{3+}$, and $Pb^{2+}$. The VBM shifts to lower B.E. as a result of the larger cation.

## 5.4 Nanocrystal Halides

Along with the rapid development of bulk perovskite deposited with solution process techniques, the research into colloidal perovskite nanocrystals (CPNs) has also emerged very recently with favorable results[146]. The potential for CPNs are enormous, as colloidal quantum dots (CQDs) have already been building block components to light emitting devices (LEDs), photodetectors, and solar cells[56,147]. We recently reported on a one of the best-performing CPNs-based solar cell using $CsPbI_3$ and PbS as functional units in the light-harvesting layer of the photovoltaic devices[55]. The material is based on $CsPbI_3$ CQDs grown directly on top of an optically active PbS CQD – an architecture that is coined '*core-shell quantum dot structure*' that results in an observable quantum-confinement effect[148]. This work is reported in Paper X and only the relevant results will be discussed here.

Figure 5.9 displays the core electronic levels and the valence band for three systems: oleic-acid capped PbS (PbS-OA), $PbI_2$ shell and PbS core CQD (PbS-$PbI_2$), and the HP $CsPbI_3$ grown on a core PbS (PbS-$CsPbI_3$). The core-levels (Pb 4*f*, Cs 4*d*, I4*d*) are normalized to the S 2*p* extending from the PbS underlayer. Based on the S 2*p* ratio with respect to Pb 4*f* core-level signals

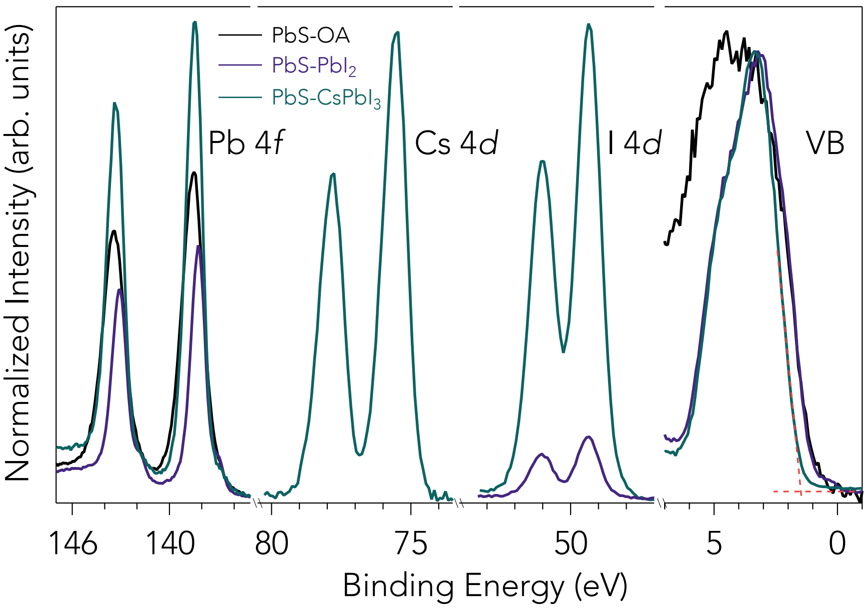

*Figure 5.9* Core level x-ray photoelectron spectra normalized to S 2*p* signal of Pb 4*f*, Cs 4*d*, I 4*d* for the PbS-$PbI_2$ and PbS-$CsPbI_3$-P based CQD solids, respectively, and valence band spectra (normalized to maximum intensity).

for the PbS-OA CQD sample, an approximation of the shell materials stoichiometry can be made. Comparing the additional Pb 4*f* signal in PbS-$CsPbI_3$-P to the intensity of the I 4*d* and using theoretical photoionization cross-sections[149], we obtain a stoichiometric ratio of I/Pb = 3.1 and I/Cs = 2.7, agreeing with the expected stoichiometry. The relative intensities of the Pb 4*f* signal, when compared against the Pb 4*f* intensity from PbS-OA sample, points to a very thin surface layer for $PbI_2$ and much stronger for $CsPbI_3$. Only minor core-level shifts in the S 2*p* and Pb 4*f* signal of PbS-$CsPbI_3$ (~ 0.15 and 0.06 eV respectively) are observed, suggesting that no large dipole layer exist at the interface of PbS/$CsPbI_3$ CQDs. In addition, the relative position of the valence band maximum (indicated by dashed lines) is shifted to lower binding energy for PbS-$CsPbI_3$ by ≈ 0.4 eV versus the Fermi level in comparison to the other two samples. Since the capping $CsPbI_3$ layer contributes significantly to the overall measured signal, the edge shift is therefore likely from the capping $CsPbI_3$ layer. This suggest that the VB edge of $CsPbI_3$ is 0.4 eV further away from the Fermi level that that of PbS-OA, which together with the absorption properties and work function measurements (*see Paper X*) indicate electronic energy levels that favor charges carrier confinement.

# 6 Outlook

This thesis presented the versatility of two classes of compounds through x-ray spectroscopic and thin film characterization. A number of complimentary techniques along with different levels of theory were applied in order to describe the electronic structure and relate the spectroscopic information to their macroscopic properties.

In order to develop a more detailed picture of $LaFe_{1-x}Mo_xO_3$ unusual ground state antiferromagnetism with metallicity could be through $K_\beta$ x-ray emission spectroscopy and Fe *K* edge RIXS. A more complex understanding on the charge disproportionation could be understood by describing the nominal spin state for the two separate Fe species in the metallic compounds. This could further validate the disproportionation observed at the Fe site. Additionally, fabrication of thin films would be the obvious next step to definitely validate metallicity at low temperatures without the complications from grain boundary effects that smear the inherent bulk properties of the materials.

The most promising outlook in the entire series of compounds studied in this thesis is perhaps in the development of $BaTi_{1-x}(Mn_{1/2}Nb_{1/2})_xO_3$ ferroelectrics. Thin films have already been fabricated and characterized with promising results. The next step would be to incorporate the films into photovoltaic devices to determine if the inherent polarization and the reduced bandgap can result in efficient devices. For a more fundamental understanding, the role of $d^0$ $Nb^{5+}$ is still unclear other than its charge-compensating role in the unit cell. EXAFS studies at the Nb *K* edge could determine if this dopant is also off-center at the B site, and whether other $d^0$ compounds could perhaps even increase the remnant polarization as a function of doping. These results could offer new strategies in doping ferroelectrics to achieve new functionalities in electronic devices and to energy-related applications.

# 7 Acknowledgements

I would like to start first by thanking my three advisors Prof. Dr. Olof Karis, Prof. Dr. Håkan Rensmo, and Dr. Sergei Butorin. Thank you for your guidance, patience, and mostly your support in giving me the freedom to do many different projects. I am grateful for your guidance in x-ray spectroscopy and material physics.

I of course must extend my sincere thanks and gratitude to Dr. Somnath Jana and Dr. Bertrand Philippe as my '*day-to-day*' advisors, whom were instrumental in guiding me in the principles of halide perovskite materials, oxide materials, and x-ray spectroscopy. Your support is truly appreciated.

I also extend my thanks to colleagues Shyam and Soham from the Indian Institute of Science whom provided me with very interesting samples and valuable discussions. I hope that we can continue to develop the BTMNO project further and to finally realize our goals of incorporating the material into functioning devices. Tremendous thanks to Dr. Soham Mukherjee for helping and guiding me through the grind and grit in the last year.

The thin film BTO project would not have been possible without the support of Henri Frederiksen and Dr. Alexei Kalaboukhov at Chalmers University. Thanks for all your incredible assistance in realizing this project. I am indebted to you for introducing me to Pulsed Laser Deposition and thin film characterization.

Much of the perovskite halide studies would not be possible without support from colleagues at KTH. Thank you Majid and Dr. Gardner for involving me in on your projects early on in the PhD. I must also thank Sagar Jain, Malin B. Johansson, and Xiaoliang Zhang who have given me many unique samples to study and wonderful discussions, and there is still more work to be done.

It was a great pleasure working with Dr. Tomas Edvinsson and Dr. Meysam Pazoki. I think we make a good team, and hope we can find the time and resources to do all the projects we've discussed over the years into the future. Thanks for all your support.

I must also thank Dr. Ute Cappel for her wonderful support in photoelectron spectroscopy. I am always learning more effective ways to be a thoughtful and efficient experimentalist at beamtimes with you, and hope to be on more with you in the future. Dr. Venkata has also give me a wonderful opportunity to work with fabrication and thin film devices, and I hope to realize our dream projects soon. Thanks very much for the involving me in your team and on some very interesting and difficult projects.

My colleagues at the Division, thank you for sharing in wonderful discussions, laughs, and your own stories over these years. I have enjoyed working with you and hope to keep the good vibes going.

To my dear family, who have always encouraged and believed in my whirlwind journey in the last few years. You are the core unit in my life.

And lastly, thank you Camilla for sharing this journey with me.

# 8 Populärvetenskaplig Sammanfattning

Behovet av alternativa energikällor blir för varje år som går en allt mer akut fråga. Trots att kostnaderna för kiselbaserade solceller för närvarande är rekordlåga finns det betydande hinder i form av tillverkningskostnader för kisel och andra tunnfilmstekniker som kan göra det allt svårare att tillräckligt minska kostnaderna för att ge en stark ekonomisk drivkraft mot förnyelsebar energi. Liknande problem finns för den mikroelektronik som är nödvändig för att möjliggöra en fortsatt utveckling av informationsteknologin, som närmar sig skalbarhetsgränsen för den nuvarande CMOS-tekniken, trots att en stor energianvändning fortfarande krävs. Vårt beroende av dessa två tekniker kräver en inriktning mot nya material som kan möta de behov vi ser i framtiden.

Det finns nya teknologier som väcker stort intresse hos forskare inom solcellsfältet där nya material används som är effektiva på att uppta solenergi och dessutom till en bråkdel av kostnaden för dagen teknologi. Detta nya fält använder halidperovskiter som är kända för sin höga ljusabsorption och goda opto-elektroniska egenskaper som kan skräddarsys för specifika ändamål. Den mest framträdande egenskapen är tillverkningsmetoden som sker i lösningar som varken kräver höga temperaturer, höga tryck eller dyrbar utrustning för tunnfilmsproduktion, vilket potentiellt kan göra produkter som baseras på dessa material avsevärt billigare.

Övergångsmetallernas oxider, i synnerhet oxider med så kallad perovskitstruktur $ABO_3$, är en lovande materialklass som uppvisar en nästan obegriplig rikedom av egenskaper som kan användas för att skapa funktionalitet på komponentnivå. Det finns en stor tilltro till att dessa typer av material har potential att möjliggöra ytterligare ökning i beräkningstätheten och energieffektiviteten hos kretsar. Utvecklingen inom beläggning av mycket tunna oxidfilmer, tillverkning av heterostrukturer och karaktäriseringsmetoder har fört oss in i en ny era där komplexa oxider kan användas för multifunktionella komponenter. Denna avhandling har studerat en speciell form av dopade ferroelektriska filmer som växts genom att deponera material under kontrollerad miljö med hjälp av intensiva pulsade lasrar. Detta system är särskilt intressant då det visar att det är möjligt att växa modifierade ferroelektriska material i tunnfilmsform med i stort bibehållna egenskaper med hjälp av denna metod. Att kunna åstadkomma ett ferroelektriskt material med ett

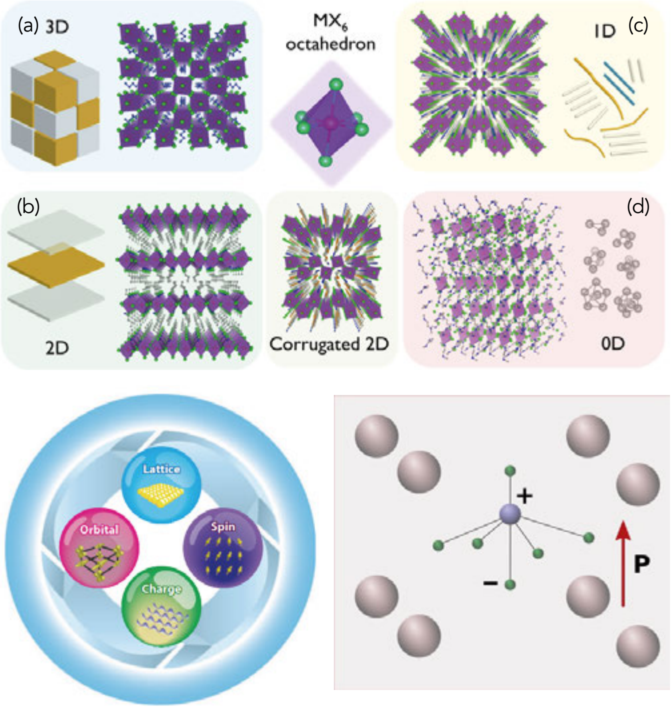

*Figure 8.1* (a) De många olika former som metallhalider med perovskitstruktur kan anta. (b) I oxidmaterial har det visat sig vara möjligt att koppla samman flera olika frihetsgrader vilket kan leda till att en egenskap kan kontrolleras genom att manipulera en annan. Ett eftersökt exempel är att styra det magnetiska tillståndet med en elektrisk spänning. Sådan funktionalitet gör dessa material intressanta för olika tillämpningar. (c) I ett ferroelektriskt material kan polarisationen (fördelningen av positivt och negativt laddade joner) ändras på ett bestående sätt med en pålagd spänning.

mindre så kallat gap, vilket möjliggör att en större del av del tillgängliga energin i solljuset skulle kunna omvandlas till elektrisk energi, i form av en tunnfilm är mycket relevant för att kunna skapa nya solceller där ett av de grundläggande problemen i cellen, laddningsseparation, sköts av den inneboende polarisationen i dessa material.

För att förstå vad som ger upphov till de så eftertraktade egenskaperna hos dessa material som gör dem relevanta för användning inom solceller och komponenter av olika slag är det mycket värdefullt att kunna studera elektronstrukturen hos materialen i detalj. Denna avhandling försöker belysa hur de unika egenskaper som gör materialen användbara i en rad tillämpningar uppkommer, genom att beskriva materialens elektronstruktur så detaljerat som möjligt. Den systematiska undersökningen av elektroniska egenskaper hos övergångsmetalloxider and metallhalider är en central del för att förstå deras egenskaper. Den grundämnes- och platsspecifika naturen hos flera röntgenbaserade spektroskopiska tekniker ges möjligheter för att få en komplett bild av de elektroniska egenskaperna hos materialen i fråga.

Hos metallhaliderna undersöks valens- och ledningsbanden med röntgenabsorption, röntgenemission och fotoelektronspektroskopi. De spektroskopiska resultaten identifierar vilka tillstånd som formar valensbandet och ledningsband, vilka är kritiska parametrar att känna till för optoelektroniska komponenter. Därutöver har röntgenbaserad spektroskopi använts för att demonsterara den stereokemiska aktiviteten för vad som benämns lone-pair tillstånd ($5s^2$ och $6s^2$) för flera olika halidföreningar och deras påverkan på de kemiska, strukturella och elektroniska egenskaperna hos materialet. Dessutom har positionerna för jodtillstånd och valensbandstillstånd i lågdimensionella bly-baserade komponenter undersökts i förhållande till sina tredimensionella motsvarigheter. Denna information belyser de intressanta materialegenskaperna och deras användning i vad som ofta benämns tredje generationens solcellsforskning.

Detta avhandlingsarbete har också behandlat flera system av funktionella oxider. Speciellt har en ny grupp av metalloxider baserade på dopning av antiferromagnetiskt $LaFeO_3$ , syntetiserats och studerats med hjälp av röntgenabsorption, röntgenemission och fotoeletronspektroskopi. Elektronstrukturen är komplex, och uppvisar både delokaliserade, eller så kallat itineranta tillstånd, såväl som lokaliserade delar som ger upphov till ett unikt tillstånd för ett material där antiferromagnetism, metallicitet och laddningsdisproportionering samexisterar. Med resultaten från resonanta fotoemission kan vi bestämma att Fe-tillstånden i de båda magnetiskt ordnade oxiderna inte bidrar till ledningsförmågan, medans molybdentillstånden uppvisar en intinerat karaktär vid Ferminivån. En undersökning utförd med resonant inelastisk röntgenspridning på $LaFe_{1-x}Mo_xO_3$ och dubbelperovskiten $Sr_2FeMoO_6$ uppvisar strukturer som vi har kunnat tolka som excitationer inom tillstånd av d-karaktär, s.k. d-d-excitationer, vilket visar på den starkt korrelerade naturen av dessa övergångsmetallmaterial.

# 9 References

1. Moore, G. E. Lithography and the future of Moore's law. *Proc. SPIE* **2437,** (1995).
2. Andrae, A. & Edler, T. On Global Electricity Usage of Communication Technology: Trends to 2030. *Challenges* **6,** 117–157 (2015).
3. Ramirez, A. P. Oxide electronics emerge. *Science* **315,** 1377–1378 (2007).
4. Ha, S. D. & Ramanathan, S. Adaptive oxide electronics: A review. *J. Appl. Phys.* **110,** (2011).
5. Salahuddin, S., Ni, K. & Datta, S. The era of hyper-scaling in electronics. *Nat. Electron.* **1,** 442–450 (2018).
6. Butler, K. T., Frost, J. M. & Walsh, A. Ferroelectric materials for solar energy conversion: Photoferroics revisited. *Energy Environ. Sci.* **8,** 838–848 (2015).
7. Nechache, R. *et al.* Bandgap tuning of multiferroic oxide solar cells. *Nat. Photonics* **9,** 61–67 (2014).
8. Xu, X., Randorn, C., Efstathiou, P. & Irvine, J. T. S. A red metallic oxide photocatalyst. *Nat. Mater.* **11,** 595–598 (2012).
9. Montoya, J. H., Doyle, A. D., Nørskov, J. K. & Vojvodic, A. Trends in adsorption of electrocatalytic water splitting intermediates on cubic ABO3oxides. *Phys. Chem. Chem. Phys.* **20,** 3813–3818 (2018).
10. Lorenz, M. *et al.* The 2016 oxide electronic materials and oxide interfaces roadmap. *J. Phys. D. Appl. Phys.* **49,** (2016).
11. Green, M. A., Ho-Baillie, A. & Snaith, H. J. The emergence of perovskite solar cells. *Nat. Photonics* **8,** 506–514 (2014).
12. Zhang, W., Eperon, G. E. & Snaith, H. J. Metal halide perovskites for energy applications. *Nat. Energy* 16048 (2016).
13. Louwen, A., Van Sark, W., Schropp, R. & Faaij, A. A cost roadmap for silicon heterojunction solar cells. *Sol. Energy Mater. Sol. Cells* **147,** 295–314 (2016).
14. Chen, H.-W., Lee, J.-H., Lin, B.-Y., Chen, S. & Wu, S.-T. Liquid crystal display and organic light-emitting diode display: present status and future perspectives. *Light Sci. Appl.* **7,** 17168 (2018).
15. Serrano-Lujan, L. *et al.* Tin- and lead-based perovskite solar cells under scrutiny: An environmental perspective. *Adv. Energy Mater.* **5,** (2015).
16. Babayigit, A., Ethirajan, A., Muller, M. & Conings, B. Toxicity of organometal halide perovskite solar cells. *Nature Materials* **15,** 247–251 (2016).
17. Babayigit, A. *et al.* Assessing the toxicity of Pb- and Sn-based perovskite solar cells in model organism Danio rerio. *Sci. Rep.* **6,** 18721 (2016).

18. Leijtens, T. *et al.* Stability of Metal Halide Perovskite Solar Cells. *Adv. Energy Mater.* **5,** 1500963 (2015).
19. Quan, L. N. *et al.* Ligand-Stabilized Reduced-Dimensionality Perovskites. *J. Am. Chem. Soc.* **138,** 2649–2655 (2016).
20. Boix, P. P., Agarwala, S., Koh, T. M., Mathews, N. & Mhaisalkar, S. G. Perovskite solar cells: Beyond methylammonium lead iodide. *J. Phys. Chem. Lett.* **6,** 898–907 (2015).
21. Ganose, A. M., Savory, C. N. & Scanlon, D. O. Beyond methylammonium lead iodide: prospects for the emergent field of ns2 containing solar absorbers. *Chem. Commun.* **53,** 20–44 (2017).
22. Shi, Z. *et al.* Lead-Free Organic–Inorganic Hybrid Perovskites for Photovoltaic Applications: Recent Advances and Perspectives. *Adv. Mater.* **29,** (2017).
23. Walsh, A. Principles of Chemical Bonding and Band Gap Engineering in Hybrid Organic-Inorganic Halide Perovskites. *J. Phys. Chem. C* **119,** 5755–5760 (2015).
24. Niesner, D. *et al.* Giant Rashba Splitting in CH3NH3PbBr3 Organic-Inorganic Perovskite. *Phys. Rev. Lett.* **117,** 126401 (2016).
25. Khomskii, D. I. *Transition metal compounds*. *Transition Metal Compounds* (Cambridge University Press, 2014). doi:10.1017/CBO9781139096782
26. Imada, M., Fujimori, A. & Tokura, Y. Metal-insulator transitions. *Rev. Mod. Phys.* **70,** 1039–1263 (1998).
27. Tokura, Y., Tokura, Y. & Nagaosa, N. Orbital Physics in Transition-Metal Oxides. *Science* **288,** 462–468 (2010).
28. Chakhalian, J., Freeland, J. W., Millis, A. J., Panagopoulos, C. & Rondinelli, J. M. Colloquium: Emergent properties in plane view: Strong correlations at oxide interfaces. *Rev. Mod. Phys.* **86,** (2014).
29. Zhang, J. & Averitt, R. D. Dynamics and Control in Complex Transition Metal Oxides. *Annu. Rev. Mater. Res.* **44,** 19–43 (2014).
30. Sawatzky, G.A., Zaanen, J., Allen, J. W. Band Gaps and Electronic Structure of Transition-Metal Compounds. *Phys. Rev. Lett.* **55,** 418–421 (1985).
31. Torrance, J. B., Lacorro, P., Asavaroengchai, C. & Metzger, R. M. Simple and Perovskite Oxides of Transition-Metals : Why some are metallic, while most are insulating. *J. Solid State Chem.* **90,** 168–172 (1991).
32. Urushibara, A. *et al.* Insulator-metal transition and giant magnetoresistance in La1-xSrxMnO3. *Phys. Rev. B* **51,** 14103–14109 (1995).
33. Salamon, M. B. & Jaime, M. The physics of manganites: Structure and transport. *Rev. Mod. Phys.* **73,** 583–628 (2001).
34. Rabe, K. M., Ahn, C. H. & Triscone, J. M.-M. *Physics of Ferroelectrics A Modern Perspective*. *Springer* **105,** (Springer-Verlag Berlin Heidelberg, 2007).
35. Scott, J. F. Applications of modern ferroelectrics. *Science* **315,** 954–959 (2007).
36. Cohen, R. E. Origin of ferroelectricity in perovskite oxides. *Nature* **358,** 136–138 (1992).

37. Benedek, N. A. & Fennie, C. J. Why Are There So Few Perovskite Ferroelectrics. *J. Phys. Chem. C* **117,** 13339–13349 (2013).
38. Fridkin, V. M. Bulk photovoltaic effect in noncentrosymmetric crystals. *Crystallogr. Reports* **46,** 654–658 (2001).
39. Yang, S. Y. *et al.* Above-bandgap voltages from ferroelectric photovoltaic devices. *Nat. Nanotechnol.* **5,** 143–7 (2010).
40. Spanier, J. E. *et al.* Power conversion efficiency exceeding the Shockley-Queisser limit in a ferroelectric insulator. *Nat. Photonics* **10,** 611–616 (2016).
41. Xing, G. *et al.* Long-range balanced electron-and hole-transport lengths in organic-inorganic CH3NH3PbI3. *Science* **342,** 344–347 (2013).
42. Stranks, S. D. & Snaith, H. J. Metal-halide perovskites for photovoltaic and light-emitting devices. *Nat. Nanotechnol.* **10,** 391–402 (2015).
43. Lee, M. M., Teuscher, J., Miyasaka, T., Murakami, T. N. & Snaith, H. J. Efficient hybrid solar cells based on meso-superstructured organometal halide perovskites. *Science* **338,** 643–7 (2012).
44. Yang, W. S. *et al.* Iodide management in formamidinium-lead-halide-based perovskite layers for efficient solar cells. *Science* **356,** 1376–1379 (2017).
45. Grätzel, M. The light and shade of perovskite solar cells. *Nat. Mater.* **13,** 838–842 (2014).
46. Jung, H. S. & Park, N.-G. Perovskite Solar Cells: From Materials to Devices. *Small* **11,** 10–25 (2014).
47. Zhou, C., Lin, H., Lee, S., Chaaban, M. & Ma, B. Organic–inorganic metal halide hybrids beyond perovskites. *Mater. Res. Lett.* **6,** 552–569 (2018).
48. Loi, M. A. & Hummelen, J. C. Hybrid solar cells: Perovskites under the Sun. *Nat. Mater.* **12,** 1087–9 (2013).
49. Goldschmidt, V. M. Die Gesetze der Krystallochemie. *Naturwissenschaften* **14,** 477–485 (1926).
50. Saparov, B. & Mitzi, D. B. Organic-Inorganic Perovskites: Structural Versatility for Functional Materials Design. *Chem. Rev.* **116,** 4558–4596 (2016).
51. Gao, P., Grätzel, M. & Nazeeruddin, M. K. Organohalide lead perovskites for photovoltaic applications. *Energy Environ. Sci.* **7,** 2448–2463 (2014).
52. Lindblad, R. *et al.* Electronic structure of CH3NH3PbX3 perovskites: Dependence on the halide moiety. *J. Phys. Chem. C* **119,** 1818–1825 (2015).
53. Brandt, R. E., Stevanović, V., Ginley, D. S. & Buonassisi, T. Identifying defect-tolerant semiconductors with high minority-carrier lifetimes: beyond hybrid lead halide perovskites. *MRS Commun.* **5,** 1–11 (2015).
54. Walsh, A., Payne, D. J., Egdell, R. G. & Watson, G. W. Stereochemistry of post-transition metal oxides: revision of the classical lone pair model. *Chem. Soc. Rev.* **40,** 4455–4463 (2011).
55. Zhang, X. *et al.* Inorganic CsPbI3 Perovskite Coating on PbS Quantum Dot for Highly Efficient and Stable Infrared Light Converting Solar Cells. *Adv. Energy Mater.* **8,** 1702049 (2017).
56. Carey, G. H. *et al.* Colloidal Quantum Dot Solar Cells. *Chemical Reviews* **115,** 12732–12763 (2015).

57. Kim, Y. *et al.* Efficient Luminescence from Perovskite Quantum Dot Solids. *ACS Appl. Mater. Interfaces* **7,** 25007–25013 (2015).
58. Yang, Z. *et al.* Colloidal Quantum Dot Photovoltaics Enhanced by Perovskite Shelling. *Nano Lett.* **15,** 7539–7543 (2015).
59. Ishii, H., Sugiyama, K., Ito, E. & Seki, K. Energy Level Alignment and Interfacial Electronic Structures at Organic/Metal and Organic/Organic Interfaces. *Adv. Mater.* **11,** 605–625 (1999).
60. Schulz, P. *et al.* Interface energetics in organo-metal halide perovskite-based photovoltaic cells. *Energy Environ. Sci.* **7,** 1377 (2014).
61. De Groot, F. M. F. & Kotani, A. *Core Level Spectroscopy of Solids*. **136,** (CRC Press, 2008).
62. Clarke, J. A. *The Science and Technology of Undulators and Wigglers. Oxford Series on Synchrotron Radiation* (Oxford University Press, 2004).
63. Brühwiler, P. A., Karis, O. & Mårtensson, N. Charge-transfer dynamics studied using resonant core spectroscopies. *Rev. Mod. Phys.* **74,** 703–740 (2002).
64. Wadati, H. *et al.* Utility of the inverse partial fluorescence for electronic structure studies of battery materials. *Appl. Phys. Lett.* **100,** 98–101 (2012).
65. Achkar, A. J. *et al.* Bulk sensitive x-ray absorption spectroscopy free of self-absorption effects. *Phys. Rev. B* **83,** 2–5 (2011).
66. De Groot, F., Vankó, G. & Glatzel, P. The 1s x-ray absorption pre-edge structures in transition metal oxides. *J. Phys. Condens. Matter* **21,** 104207 (2009).
67. Glatzel, P. & Bergmann, U. High resolution 1s core hole X-ray spectroscopy in 3d transition metal complexes - Electronic and structural information. *Coord. Chem. Rev.* **249,** 65–95 (2005).
68. Bauer, M. HERFD-XAS and valence-to-core-XES: new tools to push the limits in research with hard X-rays? *Phys. Chem. Chem. Phys.* **16,** 13827–37 (2014).
69. Bergmann, U. & Glatzel, P. X-ray emission spectroscopy. *Photosynth. Res.* **102,** 255–266 (2009).
70. Gallo, E. & Glatzel, P. Valence to core X-ray emission spectroscopy. *Adv. Mater.* **26,** 7730–7746 (2014).
71. Kotani, A. & Shin, S. Resonant inelastic x-ray scattering spectra for electrons in solids. *Rev. Mod. Phys.* **73,** 203–246 (2001).
72. Ament, L. J. P., van Veenendaal, M., Devereaux, T. P., Hill, J. P. & Brink, J. van den. Resonant Inelastic X-ray Scattering Studies of Elementary Excitations. *Rev. Mod. Phys.* **83,** 705–767 (2010).
73. Ishii, K., Tohyama, T. & Jun'ichiro Mizuki. Inelastic X-ray scattering studies of electronic excitations. *J. Phys. Soc. Japan* **82,** 1–24 (2013).
74. Jia, C., Wohlfeld, K., Wang, Y., Moritz, B. & Devereaux, T. P. Using RIXS to uncover elementary charge and spin excitations. *Phys. Rev. X* **6,** 1–16 (2016).
75. Willmott, P. R. & Huber, J. R. Pulsed laser vaporization and deposition. *Rev. Mod. Phys.* **72,** 315–328 (2000).
76. Ohring, M. *The Materials Science of Thin Films*. (Academic Press, 2013).

77. Gruverman, A. & Kholkin, A. Nanoscale ferroelectrics: Processing, characterization and future trends. *Reports Prog. Phys.* **69,** 2443–2474 (2006).

78. Jesse, S., Lee, H. N. & Kalinin, S. V. Quantitative mapping of switching behavior in piezoresponse force microscopy. *Rev. Sci. Instrum.* **77,** (2006).

79. Gruverman, A. & Kalinin, S. V. in *Frontiers of Ferroelectricity: A Special Issue of the Journal of Materials Science* 107–116 (2007).

80. Jesse, S., Baddorf, A. P. & Kalinin, S. V. Dynamic behaviour in piezoresponse force microscopy. *Nanotechnology* **17,** 1615–1628 (2006).

81. Jana, S. *et al. Doping induced site-selective Mott insulating phase in LaFeO3 (Submitted)*. (2018).

82. Kobayashi, K. I., Kimura, T., Sawada, H., Terakura, K. & Tokura, Y. Room-temperature magnetoresistance in an oxide material with an ordered double-perovskite structure. *Nature* **395,** 677–680 (1998).

83. Žutić, I., Fabian, J. & Sarma, S. Das. Spintronics: Fundamentals and applications. *Reviews of Modern Physics* **76,** 323–410 (2004).

84. Jungwirth, T., Marti, X., Wadley, P. & Wunderlich, J. Antiferromagnetic spintronics. *Rev. Mod. Phys.* **90,** 15005 (2018).

85. Hwang, H. Y., Cheong, S.-W., Ong, N. P. & Batlogg, B. Spin-Polarized Intergrain Tunneling in La2/3Sr1/3MnO3. *Phys. Rev. Lett.* **77,** 2041–2044 (1996).

86. Wadati, H. *et al.* Hole-doping-induced changes in the electronic structure of La 1-xSr x-FeO 3: Soft x-ray photoemission and absorption study of epitaxial thin films. *Phys. Rev. B* **71,** 1–7 (2005).

87. Kleibeuker, J. E. *et al.* Electronic reconstruction at the isopolar LaTiO3/LaFeO3 interface: An X-ray photoemission and density-functional theory study. *Phys. Rev. Lett.* **113,** (2014).

88. Cui, Z. *et al.* Resonant inelastic x-ray scattering study of Bi6Fe2Ti3O18, Bi6FeCoTi3O18, and LaBi5FeCoTi3O18 Aurivillius-phase oxides. *Phys. Rev. B* **95,** 205102 (2017).

89. Nomura, T. *et al.* Resonant inelastic x-ray scattering study of entangled spin-orbital excitations in superconducting PrFeAsO0.7. *Phys. Rev. B* **94,** 1–9 (2016).

90. Monney, C. *et al.* Resonant inelastic x-ray scattering at the Fe L3 edge of the one-dimensional chalcogenide Ba2Fe2Se3. *Phys. Rev. B* **88,** 165103 (2013).

91. Bisogni, V. *et al.* Ground-state oxygen holes and the metal-insulator transition in the negative charge-transfer rare-earth nickelates. *Nat. Commun.* **7,** 1–8 (2016).

92. Ishii, K., Inami, T., Ohwada, K. & Kuzushita, K. Resonant inelastic x-ray scattering study of hole-doped manganites La1−xSrxMnO3 (x = 0.2 and 0.4). *Phys. Rev. B* **3,** 1–14 (2004).

93. Sarma, D. D., Mahadevan, P., Ray, S. & Kumar, A. Electronic Structure of Sr2FeMoO6. *Phys. Rev. Lett.* **85,** 2549–2552 (2000).

94. Martins, H. P. *et al.* X-ray absorption study of the Fe and Mo valence states in Sr2FeMoO6. *J. Alloys Compd.* **640,** 511–516 (2015).

95. Martins, H. P. *et al.* Bulk-sensitive Mo 4d electronic structure of Sr2FeMoO6 probed by high-energy Mo L3 resonant photoemission. *Europhys. Lett.* **118,** 37002 (2017).
96. Martins, H. P. *et al.* Many-body effects and non-local charge fluctuations in the double perovskite Sr2FeMoO6. *RSC Adv.* **8,** 3928–3933 (2018).
97. Ray, S. *et al.* Electronic and magnetic structures of Sr2FeMoO6. *Phys. Rev. Lett.* **87,** 972041–972044 (2001).
98. Fang, Z., Terakura, K. & Kanamori, J. Strong ferromagnetism and weak antiferromagnetism in double perovskites: Sr2FeMO6(M = Mo, W, and Re). *Phys. Rev. B* **63,** 3–6 (2001).
99. De Groot, F. M. F., Fuggle, J. C., Thole, B. T. & Sawatzky, G. A. 2p x-ray absorption of 3d transition-metal compounds: An atomic multiplet description including the crystal field. *Phys. Rev. B* **42,** 5459–5468 (1990).
100. De Groot, F. M. F. *et al.* Differences between L3 and L2 x-ray absorption spectra of transition metal compounds. *J. Chem. Phys.* **101,** 6570–6576 (1994).
101. Miyawaki, J. *et al.* Dzyaloshinskii-Moriya interaction in α-Fe2O3 measured by magnetic circular dichroism in resonant inelastic soft x-ray scattering. *Phys. Rev. B* **96,** 214420 (2017).
102. Dawber, M., Rabe, K. M. & Scott, J. F. Physics of thin-film ferroelectric oxides. *Rev. Mod. Phys.* **77,** 1083–1130 (2005).
103. Martin, L. W. & Rappe, A. M. Thin-film ferroelectric materials and their applications. *Nat. Rev. Mater.* **2,** 1–15 (2016).
104. Young, S. M. & Rappe, A. M. First principles calculation of the shift current photovoltaic effect in ferroelectrics. *Phys. Rev. Lett.* **109,** 116601 (2012).
105. Zenkevich, A. *et al.* Giant bulk photovoltaic effect in thin ferroelectric BaTiO3 films. *Phys. Rev. B - Condens. Matter Mater. Phys.* **90,** 161409(R) (2014).
106. Lopez-Varo, P. *et al.* Physical aspects of ferroelectric semiconductors for photovoltaic solar energy conversion. *Phys. Rep.* **653,** 1–40 (2016).
107. Das, S. *et al.* Designing a Lower Band Gap Bulk Ferroelectric Material with a Sizable Polarization at Room Temperature. *ACS Energy Lett.* **3,** 1176–1182 (2018).
108. Arima, T., Tokura, Y. Variation of optical gaps in perovskite-type Bd transition-metal oxides. *Phys. Rev. B* **48,** 17006–17009 (1993).
109. Hill, N. a. Why Are There so Few Magnetic Ferroelectrics? *J. Phys. Chem. B* **104,** 6694–6709 (2000).
110. Vedrinskii, R. V, Kraizman, V. L., Novakovich, A. A., Demekhin, P. V & Urazhdin, S. V. Pre-edge fine structure of the 3d atom K x-ray absorption spectra and quantitative atomic structure determinations for ferroelectric perovskite structure crystals Pre-edge fine structure of the 3d atom K x-ray absorption spectra and quantitative atomic st. *J. Phys. Condens. Matter* **10,** 9561–9580 (1998).
111. Yamamoto, T., Mizoguchi, T. & Tanaka, I. Core-hole effect on dipolar and quadrupolar transitions of SrTiO3 and BaTiO3 at Ti K edge. *Phys. Rev. B* **71,** 245113 (2005).

112. Levin, I. *et al.* Local structure of Ba(Ti,Zr)O3 perovskite-like solid solutions and its relation to the band-gap behavior. *Phys. Rev. B* **83,** 94112 (2011).
113. Rabuffetti, F. A. & Brutchey, R. L. Local Structure of Ba1− xSrxTiO3 and BaTi1− yZryO3 Nanocrystals Probed by X-ray Absorption and X-ray Total Scattering. *ACS Nano* **7,** 11435–11444 (2013).
114. Visinoiu, A., Scholz, R., Chattopadhyay, S., Alexe, M. & Hesse, D. Formation of epitaxial BaTiO3/SrTiO3 multilayers grown on Nb-doped SrTiO3 (001) substrates. *Japanese J. Appl. Physics, Part 1 Regul. Pap. Short Notes Rev. Pap.* **41,** 6633–6638 (2002).
115. Ramana, E. V. *et al.* Ferroelectric and magnetic properties of Fe-doped BaTiO3thin films grown by the pulsed laser deposition. *J. Appl. Phys.* **113,** (2013).
116. Phuyal, D. *et al.* The origin of low bandgap and ferroelectricity of a co-doped (Accepted). *Europhys. Lett.* (2018).
117. Rodriguez, B. J., Jesse, S., Alexe, M. & Kalinin, S. V. Spatially resolved mapping of polarization switching behavior in nanoscale ferroelectrics. *Adv. Mater.* **20,** 109–114 (2008).
118. Balke, N., Bdikin, I., Kalinin, S. V. & Kholkin, A. L. Electromechanical imaging and spectroscopy of ferroelectric and piezoelectric materials: State of the art and prospects for the future. *J. Am. Ceram. Soc.* **92,** 1629–1647 (2009).
119. Gruverman, A. *et al.* Tunneling electroresistance effect in ferroelectric tunnel junctions at the nanoscale. *Nano Lett.* **9,** 3539–3543 (2009).
120. Shin, Y. J. *et al.* Interface Control of Ferroelectricity in an SrRuO3/BaTiO3/SrRuO3Capacitor and its Critical Thickness. *Adv. Mater.* **29,** 1–6 (2017).
121. Li, B. S. *et al.* Pinning and depinning mechanism of defect dipoles in PMnN-PZT ceramics. *J. Phys. D. Appl. Phys.* **38,** 1107–1111 (2005).
122. Folkman, C. M. *et al.* Study of defect-dipoles in an epitaxial ferroelectric thin film. *Appl. Phys. Lett.* **96,** 2008–2011 (2010).
123. Saidaminov, M. I., Mohammed, O. F. & Bakr, O. M. Low-Dimensional-Networked Metal Halide Perovskites: The Next Big Thing. *ACS Energy Letters* **2,** 889–896 (2017).
124. Hong, K., Le, Q. Van, Kim, S. Y. & Jang, H. W. Low-dimensional halide perovskites: Review and issues. *J. Mater. Chem. C* **6,** 2189–2209 (2018).
125. Tsai, H. *et al.* High-efficiency two-dimensional Ruddlesden–Popper perovskite solar cells. *Nature* **536,** 312–316 (2016).
126. Kamminga, M. E. *et al.* Confinement Effects in Low-Dimensional Lead Iodide Perovskite Hybrids. *Chem. Mater.* **28,** 4554–4562 (2016).
127. Pedesseau, L. *et al.* Advances and Promises of Layered Halide Hybrid Perovskite Semiconductors. *ACS Nano* **10,** 9776–9786 (2016).
128. Du, K. Z. *et al.* Two-Dimensional Lead(II) Halide-Based Hybrid Perovskites Templated by Acene Alkylamines: Crystal Structures, Optical Properties, and Piezoelectricity. *Inorg. Chem.* **56,** 9291–9302 (2017).
129. Venkatesan, N. R., Labram, J. G. & Chabinyc, M. L. Charge-Carrier Dynamics and Crystalline Texture of Layered Ruddlesden-Popper Hybrid Lead Iodide Perovskite Thin Films. *ACS Energy Lett.* **3,** 380–386 (2018).

130. Even, J., Pedesseau, L. & Katan, C. Understanding quantum confinement of charge carriers in layered 2D hybrid perovskites. *ChemPhysChem* **15,** 3733–3741 (2014).
131. Umebayashi, T., Asai, K., Kondo, T. & Nakao, a. Electronic structures of lead iodide based low-dimensional crystals. *Phys. Rev. B* **67,** 155405 (2003).
132. Pedesseau, L. *et al.* Advances and Promises of Layered Halide Hybrid Perovskite Semiconductors. *ACS Nano* **10,** 9776–9786 (2016).
133. Brivio, F., Walker, A. B. & Walsh, A. Structural and electronic properties of hybrid perovskites for high-efficiency thin-film photovoltaics from first-principles. *APL Mater.* **1,** (2013).
134. Yang, S., Fu, W., Zhang, Z., Chen, H. & Li, C. Z. Recent advances in perovskite solar cells: Efficiency, stability and lead-free perovskite. *J. Mater. Chem. A* **5,** 11462–11482 (2017).
135. Lehner, A. J. *et al.* Crystal and Electronic Structures of Complex Bismuth Iodides A3Bi2I9 (A = K, Rb, Cs) Related to Perovskite: Aiding the Rational Design of Photovoltaics. *Chem. Mater.* **27,** 7137–7148 (2015).
136. Walsh, A., Payne, D. J., Egdell, R. G. & Watson, G. W. Stereochemistry of post-transition metal oxides: Revision of the classical lone pair model. *Chem. Soc. Rev.* **40,** 4455–4463 (2011).
137. Jain, S. M. *et al.* An effective approach of vapour assisted morphological tailoring for reducing metal defect sites in lead-free, (CH3NH3)3Bi2I9bismuth-based perovskite solar cells for improved performance and long-term stability. *Nano Energy* **49,** 614–624 (2018).
138. Jain, S. M. *et al.* Vapor phase conversion of PbI2 to CH3NH3PbI3 : spectroscopic evidence for formation of an intermediate phase. *J. Mater. Chem. A* **4,** 2630–2642 (2016).
139. Scofield, J. H. *Theoretical Photoionization Cross Sections from 1 to 1500 keV. Lawrence Livermore Laboratory* (University of California-Livermore, 1973). doi:10.2172/4545040
140. Zhang, W. *et al.* Enhanced optoelectronic quality of perovskite thin films with hypophosphorous acid for planar heterojunction solar cells. *Nat. Commun.* **6,** 10030 (2015).
141. Park, B.-W. *et al.* Bismuth Based Hybrid Perovskites A3Bi2I9 (A: Methylammonium or Cesium) for Solar Cell Application. *Adv. Mater.* **27,** 6806–6813 (2015).
142. Brunetti, B., Cavallo, C., Ciccioli, A., Gigli, G. & Latini, A. On the Thermal and Thermodynamic (In)Stability of Methylammonium Lead Halide Perovskites. *Sci. Rep.* **6,** (2016).
143. Huang, X., Huang, S., Biswas, P. & Mishra, R. Band Gap Insensitivity to Large Chemical Pressures in Ternary Bismuth Iodides for Photovoltaic Applications. *J. Phys. Chem. C* **120,** 28924–28932 (2016).
144. Saparov, B. *et al.* Thin-film preparation and characterization of Cs3Sb2I9: A lead-free layered perovskite semiconductor. *Chem. Mater.* **27,** 5622–5632 (2015).

145. McCall, K. M., Stoumpos, C. C., Kostina, S. S., Kanatzidis, M. G. & Wessels, B. W. Strong Electron-Phonon Coupling and Self-Trapped Excitons in the Defect Halide Perovskites A3M2I9(A = Cs, Rb; M = Bi, Sb). *Chem. Mater.* **29,** 4129–4145 (2017).
146. Protesescu, L. *et al.* Nanocrystals of Cesium Lead Halide Perovskites (CsPbX3, X = Cl, Br, and I): Novel Optoelectronic Materials Showing Bright Emission with Wide Color Gamut. *Nano Lett.* **15,** 3692–3696 (2015).
147. Kagan, C. R., Lifshitz, E., Sargent, E. H. & Talapin, D. V. Building devices from colloidal quantum dots. *Science (80-. ).* **353,** (2016).
148. Reiss, P., Protière, M. & Li, L. Core/shell semiconductor nanocrystals. *Small* **5,** 154–168 (2009).
149. Scofield, J. H. Hartree-Slater Subshell Photoionization Cross-Sectionat 1254 eV and 1487 eV. *J. Electron Spectros. Relat. Phenomena* **8,** 129–137 (1976).

# Acta Universitatis Upsaliensis

*Digital Comprehensive Summaries of Uppsala Dissertations from the Faculty of Science and Technology* 1740

Editor: The Dean of the Faculty of Science and Technology

ACTA
UNIVERSITATIS
UPSALIENSIS
UPPSALA
2018

Distribution: publications.uu.se
urn:nbn:se:uu:diva-364407